PROCEEDINGS A

royalsocietypublishing.org/journal/rspa

CC BY

Research

Cite this article: Lawrie JB, Afzal M. 2026 Higher-mode filtering: optimum attenuation in a continuum of exceptional points. *Proc. R. Soc. A* **482**: 20250811.
https://doi.org/10.1098/rspa.2025.0811

Received: 17 September 2025
Accepted: 30 April 2026

Subject Areas:
wave motion, applied mathematics, acoustics

Keywords:
exceptional point, optimum attenuation, mode filtering in acoustic duct, enhanced mode matching

Author for correspondence:
Jane B. Lawrie
e-mail: Jane.Lawrie@brunel.ac.uk

Higher-mode filtering: optimum attenuation in a continuum of exceptional points

Jane B. Lawrie[1] and Muhammad Afzal[2]

[1]Department of Mathematics, Brunel University London, Uxbridge, UB8 3PH, UK
[2]Center for Applied Mathematics and Bioinformatics, Department of Mathematics and Natural Sciences, Gulf University of Science and Technology, Hawally 32093, Kuwait

JBL, 0000-0003-3674-5605

Exceptional points (EPs) occur when two (EP2) or more, say N (EPN), modes coalesce causing a collapse of the eigenbasis in the underlying eigensystem. This phenomenon, which is associated with optimal attenuation, can arise in acoustic waveguides for which the eigensystem contains two or more parameters. This study focuses on mode filtering in a horizontal, rigid waveguide comprising an inlet duct (containing a point source) and an outlet duct, together with a finite-length component containing one/two horizontal wire-mesh perforate(s). The eigensystem has three/five parameters and the aim is to determine the best configuration to filter higher-order modes leaving only the plane wave. The initial tenet is that optimum filtering corresponds to EP2 (or EP3 when present) conditions. In fact, the results are surprising. For the case of one wire-mesh perforate, there exists a non-EP configuration that can perform as well or better than the EP2 case. For two wire-mesh perforates, the eigensystem exhibits a finite number of EP3s and a continuum of EP2s. An optimum EP2 occurs when the attenuation of an EP2 mode merges with that of the next least attenuated mode. One such configuration consistently performs as well or better than an EP3 configuration.

© 2026 The Authors. Published by the Royal Society under the terms of the Creative Commons Attribution License http://creativecommons.org/licenses/by/4.0/, which permits unrestricted use, provided the original author and source are credited.

THE ROYAL SOCIETY PUBLISHING

Downloaded from http://royalsocietypublishing.org/rspa/article-pdf/doi/10.1098/rspa.2025.0811/6148136/rspa.2025.0811.pdf
by Brunel University user
on 05 July 2026

https://royalsocietypublishing.org/journal/rspa Proc. R. Soc. A 482: 20250811

1. Introduction

An exceptional point (EP) occurs when two (or more) eigenvalues, and the corresponding eigenvectors or eigenfunctions, of a given system merge causing a collapse of the eigenbasis, i.e. loss of completeness. EPs are associated with non-Hermitian systems and are found in a wide variety of physical situations including optics [1,2], open quantum systems [3], vibration [4,5] and acoustics [6]. Recollect that a square matrix is Hermitian if and only if it is equal to its conjugate transpose, and that this property ensures that the eigenvalues are real. In contrast, non-Hermitian systems usually have complex eigenvalues. A fascinating feature of non-Hermitian systems is that they can be tuned to generate phenomena that are not found in the Hermitian case, in particular, EPs [1].

Although EPs are found in a diverse range of disciplines, they are not necessarily equivalent phenomena. In many experimental and/or theoretical contexts, including particle physics, optics and electromagnetic waves, the scattering matrix is an accessible and powerful tool. An $M \times M$-dimensional scattering matrix S maps a set of waves incident towards a scattering component via M channels onto a set of outgoing waves. For a non-Hermitian system, the scattering matrix has complex elements and an EP will occur when the eigenvalues (and the associated eigenvectors) coalesce. The simplest case is a two-port system, for which the scattering matrix is 2×2. In this case, it is straightforward to write down the matrix eigenvalues in terms of the elements and determine the precise conditions for an EP to occur [7].

Scattering matrices are also widely used to analyse three-part acoustic duct problems [8]. The use of scattering matrices in this context is intrinsically a low-frequency approach, although recent developments extend its application to higher frequencies [9,10]. That notwithstanding, mode-matching (MM) methods [11–13] remain a powerful, versatile and popular alternative. This technique relies on the decomposition of the acoustic field, in each section of the waveguide, as a series of duct modes with transverse wavenumber, say, α_n, $n = 1, 2, 3, \ldots$. Orthogonality relations are used to apply appropriate continuity conditions at the duct junctions reducing the problem to that of solving an infinite system of linear equations for the modal amplitudes. This can, of course, be expressed in a matrix form. In this context, an EP occurs when two or more modes coalesce, for example when α_1 and α_2 merge (which can happen only if α_n, $n = 1, 2, 3, \ldots$ are complex). When this occurs, the MM method fails owing to the self-orthogonality of the merged mode and consequent loss of completeness of the eigenfunctions. This is manifest as degeneracies in the elements of the matrix for the modal amplitudes. Thus, while there are strong conceptual similarities between the merging of the eigenvalues of a scattering matrix and the merging of modes in acoustic waveguides, there are also subtle differences.

A classic example of an acoustic waveguide that exhibits an EP is the two-dimensional duct, lined along one wall. This was considered by Cremer [14] who showed that the optimum attenuation occurs when a mode pair degenerates into a single mode (i.e. at EP conditions). Although this study was published in 1953, it not until 20 years later that Tester [15] derived Green's function appropriate for the optimal impedance lining. Other notable work from this time includes [16,17] but otherwise Cremer's concept of optimum attenuation received little further attention until quite recently when a number of papers were published exploring the idea in the context of noise attenuation within two-dimensional, circular and/or annular ducts, for example [18–24]. Thus, by 2022, much was known about optimum attenuation and the additional functions required to reinstate completeness were also known [6,25] but little progress had been made with regard to developing analytic or semi-analytic solution methods at EP conditions. Lawrie *et al.* [11] addressed this deficiency by developing an enhanced MM method which systematically incorporated the appropriate additional functions ensuring the correct solution at EP conditions.

For this class of problem the transverse wavenumbers, α_n, are equivalent to the eigenvalues of a Sturm–Liouville boundary value problem but differ in that they can be complex and can be repeated. Further, the normalization factor for the eigenfunctions, say P_n, is directly proportional to the derivative of the characteristic equation. Thus, at a double or triple root, completeness is lost (equivalently the eigenbasis collapses) since the corresponding eigenfunction is self-orthogonal.

Downloaded from http://royalsocietypublishing.org/rspa/article-pdf/doi/10.1098/rspa.2025.0811/6148136/rspa.2025.0811.pdf
by Brunel University user
on 05 July 2026

It follows that, for this class of problem, any double zero of the characteristic equation is an EP of order two. Further, if multiple derivatives of the characteristic equation are zero at, say α_1, the order of the EP can be measured in terms of the number of additional functions (often referred to as generalized eigenfunctions [6]) required to restore completeness. In the case of the double zero this is one, for the triple zeros discussed in this article two additional functions are needed (see appendix A).

Note that the duct considered by Lawrie *et al.* [11] is two-dimensional and lined on both the top and bottom. Thus, after non-dimensionalization, there are two complex parameters μ and ν (the non-dimensionalized wall admittances) and a non-dimensional wavenumber k. Most of the paper is concerned with fixed k and the two complex parameters enable the system to be tuned to EP conditions. Owing to the number of independent parameters (essentially four), the system exhibits a finite number of isolated EP3s and a continuum of EP2s. The latter can be explained as follows. Following the convention of Perrey-Debain *et al.* [24] by using an 'overbar' to indicate EP conditions, the parameter pair $(\bar{\mu}, \bar{\nu})$ can be expressed in terms of the merged mode $\bar{\alpha}$ [11,24]. Thus, one can choose any value for $\bar{\alpha}$ and generate $(\bar{\mu}, \bar{\nu})$ such that the choice is indeed an EP2.

The aims of this paper are threefold. The first is to demonstrate the effectiveness of the enhanced MM method developed by Lawrie *et al.* [11] when applied to a three-part problem. The model problem is inspired by the work of Kuznetsova *et al.* [26] who used Comsol Multiphysics software to generate their solution. Thus, this paper addresses a three-part waveguide comprising two-dimensional rigid inlet and outlet ducts together with a finite-length middle section containing, initially, one wire-mesh perforate positioned parallel to the rigid duct walls. The structure of the wire-mesh perforate is described in detail in [27,28]. It comprises a very fine wire mesh bonded to a rigid perforate plate. The wire mesh is purely resistive and its resistance, which characterizes the lossy effect owing to the viscous friction of the creeping flow in the wire-mesh pores, is independent of frequency provided the wavenumber is much larger than the mesh thickness. The resistance of the combined structure is the product of the resistance of the wire mesh and the percentage open area of the perforate plate. Henceforth, the term wire mesh refers to the combined wire-mesh perforate structure. Forcing is introduced in the form of a point source located in the inlet duct, and the purpose of the wire mesh is to filter higher-order modes leaving only the plane wave propagating in the outlet duct.

The second aim of this paper is to ascertain whether the mode-filtering process, as described by Kuznetsova *et al.* [26], can be improved and/or extended to higher frequencies. To do this, a second wire mesh is introduced which increases the number of parameters in the problem to four real parameters (of two distinct types: resistance and position) plus the wavenumber k. The facts that the parameters are real (with two pre-multiplied by i) and that two of them occur within the argument of trigonometric terms in the characteristic equation, does increase the computational difficulty of locating, in particular, EP3s. However, as for the lined duct considered by Perrey-Debain *et al.* [24] and Lawrie *et al.* [11], the EP2s form a continuum. The plane wave is unaffected by the wire mesh and the focus is on locating the EPs that corresponds to the coalescence of the first two (or three) higher-order modes. Filtering success is measured in terms of the purity of the plane wave travelling in the outlet duct and the length of the wire mesh required to achieve this. Clearly, the shorter the wire mesh the better. Thus, the final aim is to investigate the EP2 continuum with the view to determining which EP2 parameters offer the best attenuation and, thus, the best filtering for a given frequency range.

This paper is laid out as follows. In §2, the problem is formulated and non-dimensionalized, and in §3, the case of a single wire mesh is considered. The problem is split into two sub-problems, which are symmetric and antisymmetric, respectively, about a plane through the mid-point of the duct and perpendicular to its walls. These are solved both for no EP using a standard MM method and for EP conditions using the enhanced approach [11]. Results for the full problem are easily constructed from those for the sub-problems, and those presented concur with the work of Kuznetsova *et al.* [26]. In §4, the case of two wire meshes is addressed (again by splitting the problem into symmetric and antisymmetric sub-problems) for no EP, EP2 and EP3. A thorough investigation into one particular EP2 continuum (that arising when the two wire meshes are

Downloaded from http://royalsocietypublishing.org/rspa/article-pdf/doi/10.1098/rspa.2025.0811/6148136/rspa.2025.0811.pdf
by Brunel University user
on 05 July 2026

https://royalsocietypublishing.org/journal/rspa Proc. R. Soc. A 482: 20250811

symmetrically positioned with respect to the duct midline) is executed and it is shown that for $6.188 < k < 14.4341$, where k is the non-dimensional wavenumber, the optimum EP parameters occur when the attenuation of the EP mode merges with that of the next least attenuated higher-order mode. This is a key result which should not be confused with EP3 conditions (which are also discussed). The final section presents a comprehensive discussion of the findings. In particular, it is demonstrated that: for one wire mesh at lower values of k, there exists at least one non-EP configuration that performs as well or better than the EP case; using two wire meshes filtering can be efficiently achieved for frequencies up to that corresponding to $k = 14.4341$; for all values of k considered, the optimum choice of EP2 performs as well as or better than an EP3 configuration.

2. Formulation of the model problem

Consider a two-dimensional duct of height $\hat{h}$ occupying the region $0 \le \hat{y} \le h$, $-\infty < \hat{x} < \infty$ of a Cartesian frame of reference and containing a compressible fluid of density $\hat{\rho}$ and sound speed $\hat{c}$. The horizontal walls of the waveguide are assumed to be rigid. The central region of the duct, that is, $|\hat{x}| < \hat{L}$, contains either one (§3) or two (§4) horizontal wire meshes. One wire mesh lies along $\hat{y} = \hat{d}$, $|\hat{x}| < \hat{L}$ and the second, when present, lies along $\hat{y} = \hat{b}$, $|\hat{x}| < \hat{L}$ where $\hat{d} < \hat{b} < \hat{h}$. Under the assumption of harmonic time dependence, $\mathrm{e}^{-\mathrm{i}\hat{\omega}\hat{t}}$, where $\hat{\omega} = \hat{c}\hat{k}$ is the radian frequency (in which $\hat{k}$ is the fluid wavenumber), the boundary value problem can be non-dimensionalized according to $\hat{x} = \hat{h}x$, $\hat{y} = \hat{h}y$ and $\hat{\omega}\hat{t} = t$. The non-dimensionalized physical configuration of the duct (with two wire meshes) is shown in figure 1. The governing equation is

$$(\nabla^2 + k^2)\psi = 0, \tag{2.1}$$

where $k = \hat{k}\hat{h}$. Here, $\psi(x, y)$ is the non-dimensional reduced (time-independent) fluid velocity potential, which may be expressed as follows:

$$\psi(x,y) = \begin{cases} \psi_1(x,y), & x < -\ell, \quad 0 \le y \le 1, \\ \psi_2(x,y), & |x| < \ell, \quad 0 \le y \le 1, \\ \psi_3(x,y), & x > \ell, \quad 0 \le y \le 1, \end{cases} \tag{2.2}$$

where $\hat{h}\ell = \hat{L}$. The duct has rigid boundaries at $y = 0$ and 1,

$$\frac{\partial \psi}{\partial y} = 0 \quad \text{at } y = 0, 1, \quad -\infty < x < \infty, \tag{2.3}$$

and the normal velocity across the wire mesh(es) is continuous,

$$\frac{\partial \psi_2}{\partial y}(x, y^-) = \frac{\partial \psi_2}{\partial y}(x, y^+) \quad \text{at } y = d, b, \quad -\infty < x < \infty. \tag{2.4}$$

The wire mesh, lying at $y = d$ in the region $|x| < \ell$, satisfies the following condition:

$$i\mathcal{C}_1 \frac{\partial \psi_2}{\partial y}(x, d) = \psi_2(x, d^+) - \psi_2(x, d^-), \quad \mathcal{C}_1 \in \mathbb{R} \tag{2.5}$$

and the second wire mesh satisfies

$$i\mathcal{C}_2 \frac{\partial \psi_2}{\partial y}(x, b) = \psi_2(x, b^+) - \psi_2(x, b^-), \quad \mathcal{C}_2 \in \mathbb{R}. \tag{2.6}$$

Here, $\mathcal{C}_j = R_j/k$ for $j = 1, 2$, in which R_1 and R_2 are the (real) resistances of the wire meshes lying at $y = d$ and b, respectively. Although this paper addresses only the purely resistive case, the analysis is general and applies should $\mathcal{C}_j$ be complex. (Indeed were $\mathcal{C}_j$, $j = 1, 2$ to be complex, this would increase the number of parameters in the boundary value problem and, for the case of two wire meshes, higher-order EPs, for example EP4, could possibly occur.) Forcing is introduced in the

Downloaded from http://royalsocietypublishing.org/rspa/article-pdf/doi/10.1098/rspa.2025.0811/6148136/rspa.2025.0811.pdf
by Brunel University user
on 05 July 2026

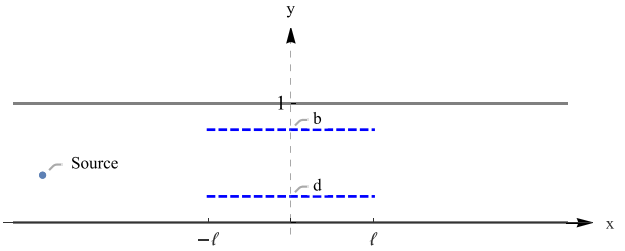

Figure 1. Duct geometry. The dashed lines indicate the wire meshes.

form of a point source located at (x_0, y_0) where $x_0 < -\ell$. The acoustic response due to the source satisfies the dimensionless wave equation

$$\left\{\frac{\partial^2}{\partial x^2} + \frac{\partial^2}{\partial y^2} + k^2\right\}\phi^i(x,y) = -F\delta(x-x_0)\delta(y-y_0), \tag{2.7}$$

where F is the forcing amplitude and $\delta(.)$ represents the Dirac delta function. Green's function for the incident field is straightforward to construct [29,30] and is given here as

$$\phi^i(x,y) = \sum_{n=0}^{\mathrm{N_I}-1} a_n(x)\,\cos(n\pi y), \tag{2.8}$$

where $\mathrm{N_I}$ represents the number of cut-on modes in the region $x < -\ell$ and

$$a_n(x) = \begin{cases} \dfrac{F\cos(n\pi y_0)}{\epsilon_n \eta_n}\,\mathrm{e}^{-\mathrm{i}\eta_n(x+\ell-x_0)}, & x+\ell < x_0, \quad k \neq n\pi, \\ \dfrac{F\cos(n\pi y_0)}{\epsilon_n \eta_n}\,\mathrm{e}^{\mathrm{i}\eta_n(x+\ell-x_0)}, & x+\ell > x_0, \quad k \neq n\pi, \end{cases} \tag{2.9}$$

in which $\eta_n = \sqrt{k^2 - n^2\pi^2}$, $n = 0, 1, 2, \ldots$, ϵ_n is 2 when $n = 0$ and 1 otherwise. Here, F is the forcing amplitude chosen such that the incident power is unity. Thus,

$$F = \sqrt{\frac{2}{\sum_{m=0}^{\mathrm{N_I}-1} \frac{\cos^2(m\pi y_0)}{\epsilon_m \eta_m}}}, \quad k \neq m\pi. \tag{2.10}$$

The incident field is reflected and transmitted at the interface $x = -\ell$ owing to the presence of the wire mesh(es) in the region at $|x| < \ell$. Further scattering occurs at $x = \ell$. The eigenfunction expansions for the reflected and transmitted fields are well known. Thus, the full potential in the inlet region $(x < -\ell)$ and the outlet region $(x > \ell)$ can be expressed as

$$\psi_1(x,y) = \sum_{n=0}^{\mathrm{N_I}-1} a_n(x)\cos(n\pi y) + \sum_{n=0}^{\infty} A_n \cos(n\pi y)\,\mathrm{e}^{-\mathrm{i}\eta_n(x+\ell)}, \quad x < -\ell \tag{2.11}$$

and

$$\psi_3(x,y) = \sum_{n=0}^{\infty} D_n \cos(n\pi y)\,\mathrm{e}^{\mathrm{i}\eta_n(x-\ell)}, \quad x > \ell, \tag{2.12}$$

where A_n and D_n are the reflected and transmitted modal amplitudes, respectively. These will be determined using MM.

3. Single wire mesh

The single wire-mesh case was considered by Kuznetsova *et al.* [26], who computed the pressure field using the Comsol Multiphysics software with perfectly matched layers in the far field to avoid reflections. In this paper, the problem is addressed using MM.

Downloaded from http://royalsocietypublishing.org/rspa/article-pdf/doi/10.1098/rspa.2025.0811/6148136/rspa.2025.0811.pdf
by Brunel University user
on 05 July 2026

https://royalsocietypublishing.org/journal/rspa Proc. R. Soc. A 482: 20250811

In the region $|x| < \ell$, the separable travelling waveforms take the form $Y(s,y)\,\mathrm{e}^{\pm \mathrm{i}sx}$ and must satisfy equations (2.1), (2.3), (2.4) and (2.5). On using the notation $Y_n(y) = Y(s_n, y)$, $n = 0, 1, 2, \ldots$ the eigenfunctions for $n > 0$ are defined piecewise by

$$Y_n(y) = \begin{cases} Y_{1,n}(y) = \cos(\alpha_n y), & 0 \le y < d, \\ Y_{2,n}(y) = \dfrac{\sin(\alpha_n d)\cos[\alpha_n(y-1)]}{\sin[\alpha_n(d-1)]}, & d < y \le 1, \end{cases} \tag{3.1}$$

where the transverse wavenumbers $\alpha_n = \sqrt{k^2 - s_n^2}$, $n = 1, 2, 3 \ldots$ are the roots of the characteristic equation

$$K(s) = \sin(\alpha) + i\mathcal{C}_1 \alpha \sin(\alpha d)\sin[\alpha(d-1)] = 0 \quad \text{with } \alpha = \sqrt{k^2 - s^2}. \tag{3.2}$$

Note that, the characteristic function defined in equation (3.2) could be viewed as a function of α (which is a function of s); however, it is more convenient to treat it as a function of s. From equation (3.2), it can easily be seen that $\alpha_0 = 0$ is the first root. This corresponds to a plane wave and, thus, $Y_0(y) = 1$. All other roots α_n for $n = 1, 2, 3, \ldots$ are complex and must be found numerically. The eigenfunctions satisfy the following orthogonality relation:

$$\int_0^1 Y_n(y) Y_m(y)\,\mathrm{d}y = P_n \delta_{mn}, \tag{3.3}$$

with

$$P_n = -\frac{Y_n'(d) K'(s_n)}{2\alpha_n \sin[\alpha_n(d-1)]}, \quad n > 0, \tag{3.4}$$

where the prime indicates differentiation with respect to the argument. A root α_n, of equation (3.2) is an EP of order two (EP2) if, for some values of n, say $n = j > 0$, $K(s_j) = K'(s_j) = 0$. At an EP, the eigenfunctions $Y_n(y)$, $n = 1, 2, 3 \ldots$ no longer form a complete set, which is indicated by the fact that $P_j = 0$. For such cases, a further non-separable waveform associated with α_j exists and must be included in the eigenfunction expansion for the potential. This will be addressed later in the text; full details of the method are given by Lawrie *et al.* [11].

(a) Standard mode-matching solution

In the absence of an EP, the eigenfunction expansion in the duct region $|x| < \ell$ is

$$\psi_2(x,y) = B_0\,\mathrm{e}^{\mathrm{i}kx} + C_0\,\mathrm{e}^{-\mathrm{i}kx} + \sum_{n=1}^{\infty} B_n Y_n(y)\,\mathrm{e}^{\mathrm{i}s_n x} + \sum_{n=1}^{\infty} C_n Y_n(y)\,\mathrm{e}^{-\mathrm{i}s_n x}. \tag{3.5}$$

Note that in equations (2.11), (2.12) and (3.5), the modal amplitudes are unknown. To find these, the matching conditions, i.e. continuity of pressure and normal velocity, are imposed at the interfaces $x = \pm\ell$, $0 \le y \le 1$. However, before applying these, it is convenient to split the problem into two sub-problems, which are symmetric and antisymmetric, respectively, about the vertical line $x = 0$.

(i) Symmetric sub-problem

The symmetric sub-problem comprises a semi-infinite, rigid duct occupying the region $x < -\ell$, $0 \le y \le 1$ together with a finite section (containing the wire mesh) in $-\ell < x \le 0$, $0 \le y \le 1$. The duct is closed by a rigid end plate ($\partial_x \psi_2 = 0$) at $x = 0$. The end-plate condition yields $C_n = B_n$ and it is convenient to define $B_n = B_n^s / \sin(s_n \ell)$ where the superscript ^{s} indicates 'symmetric'. Thus,

Downloaded from http://royalsocietypublishing.org/rspa/article-pdf/doi/10.1098/rspa.2025.0811/6148136/rspa.2025.0811.pdf
by Brunel University user
on 05 July 2026

the potentials (2.11) and (3.5) can be reformulated as

$$\psi_1^s(x,y) = \sum_{n=0}^{\mathrm{N_I}-1} a_n(x)\cos(n\pi y) + \sum_{n=0}^{\infty} A_n^s \cos(n\pi y)\,\mathrm{e}^{-\mathrm{i}\eta_n(x+\ell)}, \quad x < -\ell \tag{3.6}$$

and

$$\psi_2^s(x,y) = 2B_0^s\frac{\cos(kx)}{\sin(k\ell)} + 2\sum_{n=1}^{\infty} B_n^s \frac{\cos(s_n x)}{\sin(s_n\ell)}Y_n(y), \quad -\ell < x \le 0. \tag{3.7}$$

On considering continuity of pressure, that is, $\psi_1^s(-\ell,y) = \psi_2^s(-\ell,y)$, $0 \le y \le 1$, it is clear that

$$\sum_{n=0}^{\mathrm{N_I}-1} a_n(-\ell)\cos(n\pi y) + \sum_{n=0}^{\infty} A_n^s \cos(n\pi y) = 2B_0^s\frac{\cos(k\ell)}{\sin(k\ell)} + 2\sum_{n=1}^{\infty} B_n^s\frac{\cos(s_n\ell)}{\sin(s_n\ell)}Y_n(y). \tag{3.8}$$

On multiplying by $\cos(m\pi y)$, integrating over $0 < y < 1$ and simplifying using the orthogonality relation for $\cos(n\pi y)$, equation (3.8) becomes

$$A_m^s = -a_m(-\ell) + B_0^s\frac{4\cos(k\ell)}{\epsilon_m\sin(k\ell)}L_{m0} + \frac{4}{\epsilon_m}\sum_{n=1}^{\infty} B_n^s\frac{\cos(s_n\ell)}{\sin(s_n\ell)}L_{mn}, \tag{3.9}$$

where

$$L_{mn} = \int_0^1 \cos(m\pi y)Y_n(y)\,\mathrm{d}y. \tag{3.10}$$

Similarly, continuity of normal velocity, that is, $\psi_{2x}^s(-\ell,y) = \psi_{1x}^s(-\ell,y)$, $0 \le y \le 1$, yields

$$2B_0^s k + 2\sum_{n=1}^{\infty} B_n^s s_n Y_n(y) = \sum_{n=0}^{\mathrm{N_I}-1} a_n'(-\ell)\cos(n\pi y) - i\sum_{n=0}^{\infty} A_n^s\eta_n\cos(n\pi y), \tag{3.11}$$

where the prime implies differentiation with respect to x. On multiplying equation (3.11) by $Y_m(y)$ for $m \ge 1$, integrating over $0 < y < 1$ and using equation (3.3), it is found that

$$B_m^s = \frac{1}{2s_m P_m}\sum_{n=0}^{\mathrm{N_I}-1} a_n'(-\ell)L_{nm} - \frac{i}{2s_m P_m}\sum_{n=0}^{\infty} A_n^s\eta_n L_{nm}. \tag{3.12}$$

On multiplying equation (3.11) by $Y_0(y) = 1$ and integrating over $0 < y < 1$, it is found that

$$B_0^s = \frac{a_0'(-\ell)}{2k} - \frac{iA_0^s}{2}. \tag{3.13}$$

Thus, the symmetric amplitudes A_n^s and $B_n^s, n = 0,1,2,\ldots$ can be found by solving the linear algebraic system defined by equations (3.9), (3.12) and (3.13).

(ii) Anti-symmetric sub-problem

The anti-symmetric sub-problem is analogous to the symmetric sub-problem. The difference is that the soft (pressure release, $\psi_2 = 0$) condition is applied on the end plate at $x = 0$. On proceeding as above and using ^{a} to indicate 'anti-symmetric', potentials (2.11) and (3.5) can be reformulated as

$$\psi_1^a(x,y) = \sum_{n=0}^{\mathrm{N_I}-1} a_n(x)\cos(n\pi y) + \sum_{n=0}^{\infty} A_n^a\cos(n\pi y)\,\mathrm{e}^{-\mathrm{i}\eta_n(x+\ell)} \tag{3.14}$$

and

$$\psi_2^a(x,y) = 2iB_0^a\frac{\sin(kx)}{\cos(k\ell)} + 2i\sum_{n=1}^{\infty} B_n^a\frac{\sin(s_n x)}{\cos(s_n\ell)}Y_n(y). \tag{3.15}$$

Downloaded from http://royalsocietypublishing.org/rspa/article-pdf/doi/10.1098/rspa.2025.0811/6148136/rspa.2025.0811.pdf
by Brunel University user
on 05 July 2026

On considering continuity of pressure and normal velocity at $x=-\ell$, it is found that

$$A_m^a = -a_m(-\ell) - B_0^a \frac{4i\sin(k\ell)}{\epsilon_m \cos(k\ell)} L_{m0} - \frac{4i}{\epsilon_m} \sum_{n=1}^{\infty} B_n^a \frac{\sin(s_n\ell)}{\cos(s_n\ell)} L_{mn}, \tag{3.16}$$

$$B_m^a = \frac{1}{2is_m P_m} \sum_{n=0}^{N_I-1} a_n'(-\ell) L_{nm} - \frac{1}{2s_m P_m} \sum_{n=0}^{\infty} A_n^a \eta_n L_{nm} \tag{3.17}$$

and

$$B_0^a = \frac{a_0'(-\ell)}{2ik} - \frac{A_0^a}{2}. \tag{3.18}$$

The anti-symmetric amplitudes A_n^a and B_n^a, $n=0,1,2,\ldots$ can be found by solving the linear algebraic systems defined by equations (3.16)–(3.18).

Once the symmetric and anti-symmetric amplitudes are known, the amplitudes for the full problem can be constructed using the formulae

$$A_n = \frac{A_n^s + A_n^a}{2}, \quad D_n = \frac{A_n^s - A_n^a}{2} \tag{3.19}$$

and

$$B_n = \frac{B_n^s}{2\sin(s_n\ell)} + \frac{B_n^a}{2\cos(s_n\ell)}, \quad C_n = \frac{B_n^s}{2\sin(s_n\ell)} - \frac{B_n^a}{2\cos(s_n\ell)}. \tag{3.20}$$

(b) Enhanced mode-matching for EP2

As in the article by Kuznetsova *et al.* [26], the focus here is on the EP that corresponds to the coalescence of the first two higher-order modes such that $K(s_1)=K'(s_1)=0$. Under such circumstances, a non-separable waveform associated with α_1 exists and must be added to the set of separable waveforms in order to form a complete set. Following Evans [6], Shenderov [25] and Lawrie *et al.* [11], the additional waveform is

$$\frac{\partial}{\partial s}(Y(s,y)\,\mathrm{e}^{\pm \mathrm{i}sx})|_{s=s_1} = -\left\{\frac{s_1}{\alpha_1^2}\chi(y) \mp ixY_1(y)\right\} \mathrm{e}^{\pm \mathrm{i}s_1 x}, \tag{3.21}$$

where the piecewise continuous function $\chi(y)$ is defined by

$$\chi(y) = \begin{cases} \chi_1(y), & 0 \le y < d, \\ \chi_2(y) + \alpha_1\{d\cot(\alpha_1 d) - (d-1)\cot[\alpha_1(d-1)]\}Y_{2,1}(y), & d < y \le 1, \end{cases} \tag{3.22}$$

in which

$$\chi_1(y) = y\frac{\partial Y_{1,1}}{\partial y}(y) \quad \text{and} \quad \chi_2(y) = (y-1)\frac{\partial Y_{2,1}}{\partial y}(y).$$

Note that, by construction, $\chi(y)$ satisfies the same boundary conditions as $Y_n(y)$ but a different governing equation: namely $\chi_{yy} + \alpha_1^2\chi = -2\alpha_1^2 Y_1$. Further, see Lawrie *et al.* [11], $\chi(y)$ is orthogonal to the functions $Y_n(y)$, for $n=0$ and $n=2,3,4,\ldots$, that is,

$$\int_0^1 \chi(y)Y_n(y)\,\mathrm{d}y = Q\delta_{1n}. \tag{3.23}$$

It follows that, the correct form for the eigenfunction expansion in the region $|x|<\ell$, $0\le y\le 1$ when $K(s_1)=K'(s_1)=0$ is

$$\bar{\psi}_2(x,y) = \psi_2(x,y) + \bar{B}_1\left\{\frac{s_1}{\alpha_1^2}\chi(y) - ixY_1(y)\right\}\mathrm{e}^{\mathrm{i}s_1 x} + \bar{C}_1\left\{\frac{s_1}{\alpha_1^2}\chi(y) + ixY_1(y)\right\}\mathrm{e}^{-\mathrm{i}s_1 x},$$

where $\psi_2(x,y)$ is defined in equation (3.5), the minus sign on the right-hand side of equation (3.21) has been absorbed into $\bar{B}_1$ and $\bar{C}_1$, and the overbars are used to indicate terms (or potentials) that are associated with the EP. The expansion involves the additional constants $\bar{B}_1$ and $\bar{C}_1$ (the amplitudes of the non-separable waves) together with the unknowns B_n and C_n, $n=0,1,2,\ldots$.

Downloaded from http://royalsocietypublishing.org/rspa/article-pdf/doi/10.1098/rspa.2025.0811/6148136/rspa.2025.0811.pdf
by Brunel University user
on 05 July 2026

To find the unknown modal amplitudes, it is again convenient to consider the symmetric and antisymmetric sub-problems.

(i) Symmetric sub-problem

For the symmetric sub-problem, the condition $\partial_x \bar{\psi}_2 = 0$ is applied at $x = 0$ and thus the symmetric eigenfunction expansion for the region $|x| < \ell$, $0 \le y \le 1$ has the form

$$\bar{\psi}_2^s(x,y) = \psi_2^s(x,y) + \frac{2\bar{B}_1^s}{\sin(s_1\ell)}\left\{\frac{s_1}{\alpha_1^2}\cos(s_1 x)\chi(y) + x\sin(s_1 x)Y_1(y)\right\}, \tag{3.24}$$

where $\psi_2^s(x,y)$ is given by equation (3.7). The expression for the reflected field as defined by equation (3.6) remains valid and on applying continuity of pressure at the interface ($x = -\ell$), it is found that

$$A_m^s = -a_m(-\ell) + B_0^s\frac{4\cos(k\ell)}{\epsilon_m\sin(k\ell)}L_{m0} + \frac{4\bar{B}_1^s}{\epsilon_m}\left[\frac{s_1}{\alpha_1^2}\frac{\cos(s_1\ell)}{\sin(s_1\ell)}M_m + \ell L_{m1}\right] + \frac{4}{\epsilon_m}\sum_{n=1}^{\infty}B_n^s\frac{\cos(s_n\ell)}{\sin(s_n\ell)}L_{mn}, \tag{3.25}$$

where

$$M_m = \int_0^1 \chi(y)\cos(m\pi y)\,\mathrm{d}y. \tag{3.26}$$

To apply continuity of normal velocity at the interface, the modal expansions for velocity are equated. The results of the standard mode matching hold, that is, equation (3.12) (with the restriction that $p > 1$) and equation (3.13); however, these do not yield information for B_1^s or $\bar{B}_1^s$. An equation containing $\bar{B}_1^s$ is obtained by multiplying by $Y_1(y)$ (bearing in mind that $P_1 = 0$) and using equation (3.3), and a final coupled equation for B_1^s and $\bar{B}_1^s$ is obtained by multiplying by $\chi(y)$ and using equation (3.23). The latter two actions yield

$$2\begin{pmatrix} 0 & \frac{s_1^2}{\alpha_1^2}Q \\ \frac{s_1^2}{\alpha_1^2}Q & \frac{s_1^2}{\alpha_1^2}T + Q\Xi^+ \end{pmatrix}\begin{pmatrix} B_1^s \\ \bar{B}_1^s \end{pmatrix} = \begin{pmatrix} \sum_{n=0}^{\mathrm{N_I}-1} a_n'(-\ell)L_{n1} - i\sum_{n=0}^{\infty}A_n^s\eta_n L_{n1} \\ \sum_{n=0}^{\mathrm{N_I}-1} a_n'(-\ell)M_n - i\sum_{n=0}^{\infty}A_n^s\eta_n M_n \end{pmatrix}, \tag{3.27}$$

where Q is defined in equation (3.23),

$$T = \int_0^1 \chi^2(y)\,\mathrm{d}y \quad \text{and} \quad \Xi^+ = 1 + s_1\ell\frac{\cos(s_1\ell)}{\sin(s_1\ell)}. \tag{3.28}$$

(ii) Anti-symmetric sub-problem

For the anti-symmetric case, the eigenfunction expansion in the region $|x| < \ell$, $0 \le y \le 1$ satisfies $\bar{\psi}_2 = 0$ at $x = 0$ and has the form

$$\bar{\psi}_2^a(x,y) = \psi_2^a(x,y) + \frac{2i\bar{B}_1^a}{\cos(s_1\ell)}\left\{\frac{s_1}{\alpha_1^2}\sin(s_1 x)\chi(y) - x\cos(s_1 x)Y(\alpha_1,y)\right\}, \tag{3.29}$$

where $\psi_2^a(x,y)$ is defined in equation (3.15) and the reflected field is given in equation (3.14). On applying continuity of pressure at the interface, it is found that

$$A_m^a = -a_m(-\ell) - B_0^a\frac{4i\sin(k\ell)}{\epsilon_m\cos(k\ell)}L_{m0} - \frac{4i\bar{B}_1^a}{\epsilon_m}\left[\frac{s_1}{\alpha_1^2}\frac{\sin(s_1\ell)}{\cos(s_1\ell)}M_m - \ell L_{m1}\right] - \frac{4i}{\epsilon_m}\sum_{n=1}^{\infty}B_n^a\frac{\sin(s_n\ell)}{\cos(s_n\ell)}L_{mn}, \tag{3.30}$$

Downloaded from http://royalsocietypublishing.org/rspa/article-pdf/doi/10.1098/rspa.2025.0811/6148136/rspa.2025.0811.pdf
by Brunel University user
on 05 July 2026

whereas, the continuity of normal velocity condition yields equation (3.17) (with the restriction that $p > 1$) and equation (3.18), together with

$$2i\begin{pmatrix} 0 & \frac{s_1^2}{\alpha_1^2}Q \\ \frac{s_1^2}{\alpha_1^2}Q & \frac{s_1^2}{\alpha_1^2}T + Q\Xi^- \end{pmatrix}\begin{pmatrix} B_1^a \\ \bar{B}_1^a \end{pmatrix} = \begin{pmatrix} \sum_{n=0}^{\mathrm{N_I}-1} a_n'(-\ell)L_{n1} - i\sum_{n=0}^{\infty} A_n^a \eta_n L_{n1} \\ \sum_{n=0}^{\mathrm{N_I}-1} a_n'(-\ell)M_n - i\sum_{n=0}^{\infty} A_n^a \eta_n M_n \end{pmatrix}, \tag{3.31}$$

where

$$\Xi^- = 1 - s_1\ell\frac{\sin(s_1\ell)}{\cos(s_1\ell)}. \tag{3.32}$$

Once the symmetric and anti-symmetric amplitudes are known, the amplitudes for the full problem can be constructed using equations (3.19) and (3.20) together with

$$\bar{B}_1 = \frac{\bar{B}_1^s}{2\sin(s_1\ell)} + \frac{\bar{B}_1^a}{2\cos(s_1\ell)} \quad \text{and} \quad \bar{C}_1 = \frac{\bar{B}_1^s}{2\sin(s_1\ell)} - \frac{\bar{B}_1^a}{2\cos(s_1\ell)}. \tag{3.33}$$

(iii) Results

With the exception of $\alpha_0 = 0$, the roots, α_n, $n = 1, 2, 3, \ldots$, of the characteristic equation, equation (3.2), are complex. There exist critical pairs of the real parameters d and $\mathcal{C}_1$ that give rise to EPs. For real positive $\mathcal{C}_1$, precisely one pair of critical values corresponds to the coalescence of the first two higher modes. All other pairs correspond to the coalescence of, for example, the second and third or third and fourth higher modes. Recollect that, a root α_n, of equation (3.2) is an EP2 if $K(s_n) = \partial_s K(s_n) = 0$ where $\partial_s K(s) = -\frac{s}{\alpha}\partial_\alpha K(s)$ and

$$\partial_\alpha K(s) = \cos(\alpha) + i\mathcal{C}_1\{\sin(\alpha d)\sin[\alpha(d-1)] + \alpha\, \mathrm{d}\sin[\alpha(2d-1)]\} - \alpha\sin(\alpha d)\cos[\alpha(d-1)]. \tag{3.34}$$

On eliminating $\mathcal{C}_1$ between equations (3.2) and (3.34), for $\alpha \neq 0$, it is found that EP roots satisfy

$$\alpha\sin^2(\alpha d) - \sin(\alpha)\sin(\alpha d)\sin[\alpha(d-1)] - \alpha d\sin(\alpha)\sin[\alpha(2d-1)] = 0, \tag{3.35}$$

while $\mathcal{C}_1$, viewed as a function of α, is given by

$$\mathcal{C}_1(\alpha) = \frac{i\sin(\alpha)}{\alpha\sin(\alpha d)\sin[\alpha(d-1)]}. \tag{3.36}$$

As $\mathcal{C}_1(\alpha_1)$ must be real and positive, the EP can be found by using the bisection method to determine the value of d for which the first root of equation (3.35) satisfies $\Im(\mathcal{C}_1) = 0$. Having found the critical values of d and $\mathcal{C}_1$, the roots α_n, $n = 1, 2, 3, \ldots$ can be found by solving $K(s) = 0$, where $K(s)$ is given by equation (3.2).

In order to demonstrate the effect that EP conditions have on mode-filtering, it is useful first to present some results for the non-EP case. Note that choosing values of d such that $d \ll 1$ is not useful since, as $d \to 0$, the characteristic function tends to that for a rigid duct with no wire mesh, see equation (3.2). This is true also for $\mathcal{C}_1 \ll 1$. In figure 2, the absolute value of the potential is displayed at three different values of k and two different wire mesh heights under non-EP conditions. For each of sub-figures (a)–(d), red represents the maximum value of the modulus, which is less than one but not necessarily the same for each sub-figure. The length, ℓ, of the wire mesh is selected according to $|\exp(is_L\ell)| = 0.05$ (see the figure caption for precise values of ℓ) where s_L is the least attenuated, non-real, higher mode for the given configuration (the counter L is not to be confused with the dimensional wire mesh length $\hat{L}$). Thus, for sub-figures (a)–(c), $L = 1$ and for (d) $L = 2$. In each case, the system of equations is truncated at $N = 40$ terms and the source position is $(x_0, y_0) = (-12, 0.4)$ where the value of x_0 is chosen to lie to the left-hand side of the wire mesh. Altering y_0 does not affect the results in a qualitative sense; however, the incident modal amplitudes (including that of the plane wave) depend on y_0 and so varying this will affect the transmitted power. The filtering effect of the wire mesh is obvious in figure 2a–c, and it is also

Downloaded from http://royalsocietypublishing.org/rspa/article-pdf/doi/10.1098/rspa.2025.0811/6148136/rspa.2025.0811.pdf
by Brunel University user
on 05 July 2026

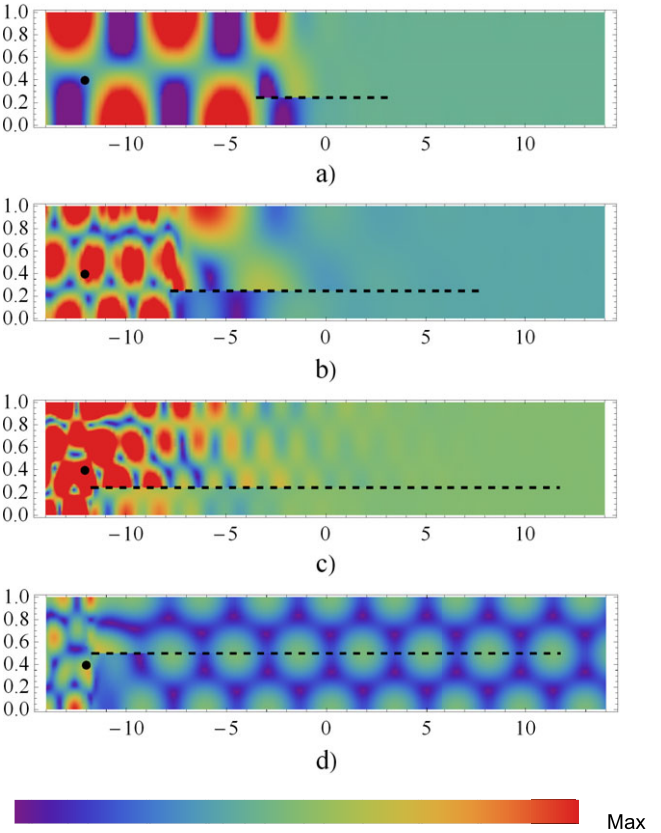

Figure 2. Absolute value of the velocity potential for one wire mesh (length 2ℓ) at non-EP conditions with $C_1 = 0.59$: (a) $k = 1.5\pi$, $\ell = 3.42$; (b) $k = 2.5\pi$, $\ell = 7.71$, (c) $k = 3.5\pi$, $\ell = 11.68$. In cases (a)–(c), $d = 0.246$ in case (d) $k = 3.5\pi$, $d = 0.5$ and $\ell = 11.68$. The dashed line and black point indicate the wire mesh and source, respectively.

clear that a longer wire mesh is required at the higher values of k to achieve the equivalent level of modal decay. In figure 2d, $d = 0.5$ and $k = 3.5$. For this combination of d and k, two of the four incident rigid duct modes have zero normal velocity on, and thus are 'invisible' to, the wire mesh (see [13] for a similar situation). It follows that, two modes are filtered while the plane mode plus the second higher mode pass through the filter with only a change of phase. Note that for this case $\ell = 11.68$ which corresponds to $|\exp(is_L\ell)| = 0.06$ with $L = 2$.

In figure 3, the absolute value of the potential is displayed for the same three values of k as in figure 2 but at EP conditions. As for the non-EP case, red represents the maximum value of the modulus, which is not necessarily the same for each sub-figure. In each case (and for all other figures in the paper unless otherwise stated), $N = 40$, $(x_0, y_0) = (-12, 0.4)$, the dashed line indicates the wire mesh and ℓ is chosen such that $|\exp(is_1\ell)| = 0.05$. At EP, the wavenumber s_1 has optimal attenuation, that is, the imaginary part is (significantly) larger than for non-EP parameters at the same value of k. Thus, for each value of k, the selection criterium leads to much shorter values of ℓ.

At a glance, the uniformity of colour for $x > \ell$ in figures 2a–c and 3 suggests that only the plane wave is propagating and filtering has been achieved. However, to further explore the quality of filtering, it is useful to consider the profile of the potential field in the region $x > \ell$. In figure 4a,b the quantity $|\psi_3(\ell + 1, y)|$ is plotted against y for non-EP and EP conditions. The zero-gradients in sub-figure (a) (non-EP) suggest that, for all frequencies considered, the potential comprises only the plane wave in the region $x > \ell$; however, the non-zero gradients of the curves in sub-figure (b) suggest that, for these values of ℓ, EP conditions produce a transmitted field which is influenced

Downloaded from http://royalsocietypublishing.org/rspa/article-pdf/doi/10.1098/rspa.2025.0811/6148136/rspa.2025.0811.pdf
by Brunel University user
on 05 July 2026

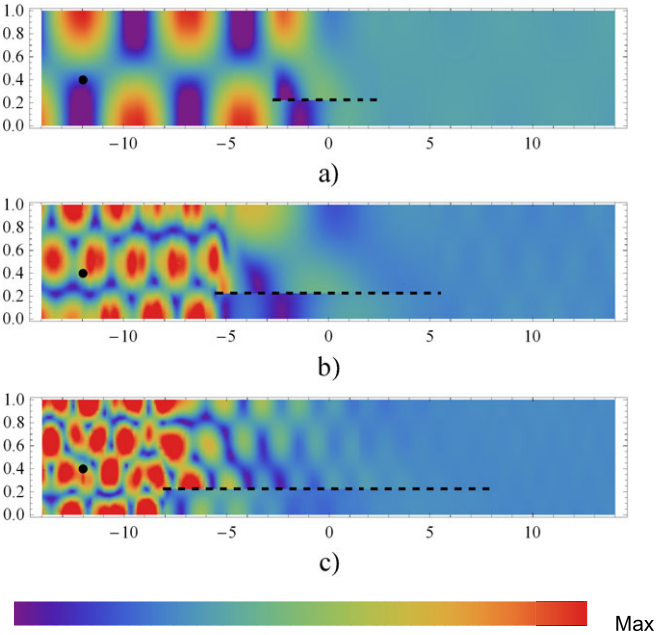

Figure 3. Absolute value of the velocity potential for one wire-mesh perforate (length 2ℓ) at EP conditions: (a) $k = 1.5\pi$, $\ell = 2.67$; (b) $k = 2.5\pi$, $\ell = 5.47$; (c) $k = 3.5\pi$, $\ell = 8.05$. In each case, $\mathcal{C}_1 = 0.476\,060$ and $d = 0.226\,591$. The the dashed line and black point indicate the wire mesh and source, respectively.

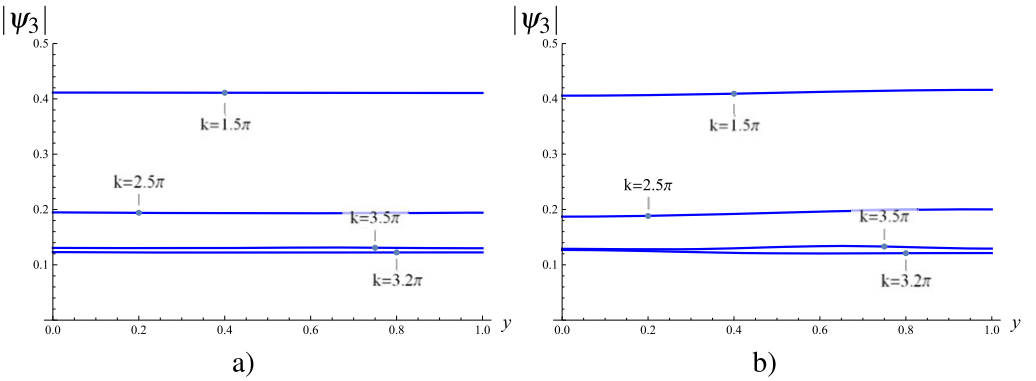

Figure 4. Absolute value of the velocity potential at $x = \ell + 1$ against y for one wire mesh (a) at non-EP conditions where $\ell = 10.52$ when $k = 3.2\pi$ and (b) at EP where $\ell = 7.29$ when $k = 3.2\pi$. All other values of ℓ are given in the captions for figures 2 and 3.

by the higher duct modes. This is thought to be due to coupling between the rigid duct modes and the additional waveform in equations (3.24) and (3.29) (which grows with x). This growth is not accounted for in the selection criterium for ℓ, which is based solely on attenuation, and higher values of ℓ are needed to improve filtering; this is discussed in §5.

Note that Kuznetsova *et al.* [26] do not consider any non-EP configurations and, for the EP case, do not consider values of k higher than 1.5π. For $k = 1.5\pi$, they take $\ell = 3.5$, which is a little larger than that used in figures 2 and 3. Whilst their choice of ℓ appears to achieve filtering, it is not clear whether it is more effective that the non-EP configuration presented in figure 2. This point is addressed in §5. Note too that, at $k \approx 3.5632533\pi$, the attenuation of the second mode is

Downloaded from http://royalsocietypublishing.org/rspa/article-pdf/doi/10.1098/rspa.2025.0811/6148136/rspa.2025.0811.pdf
by Brunel University user
on 05 July 2026

https://royalsocietypublishing.org/journal/rspa Proc. R. Soc. A 482: 20250811

equal to the EP mode attenuation and, for k greater than this value, the EP mode is no longer the least attenuated non-plane wave (this point is discussed further in the next section).

4. Two wire meshes

In this section, the case where two horizontal wire meshes are situated in the region $|x| < \ell$ is considered. As before, the separable travelling waveforms in this region take the form $Y(s,y)\,\mathrm{e}^{\pm \mathrm{i}sx}$ but must now satisfy equations (2.1), (2.3), (2.4), (2.5) and (2.6). On recollecting that $Y_n(y) = Y(s_n, y)$, $n = 0, 1, 2, \ldots$, the eigenfunctions for $n > 0$ are defined piecewise by

$$Y_n(y) = \begin{cases} Y_{1,n}(y), & 0 < y < d, \\ Y_{2,n}(y), & d < y < b, \\ Y_{3,n}(y), & b < y < 1, \end{cases} \tag{4.1}$$

in which

$$Y_{1,n}(y) = \cos(\alpha_n y), \tag{4.2}$$

$$Y_{2,n}(y) = i\mathcal{C}_1\alpha_n \sin(\alpha_n d)\cos[\alpha_n(y-d)] + \cos(\alpha_n y) \tag{4.3}$$

and

$$Y_{3,n}(y) = \frac{\Omega(\alpha_n)\cos[\alpha_n(y-1)]}{\sin[\alpha_n(1-b)]}, \tag{4.4}$$

with

$$\Omega(\alpha_n) = i\mathcal{C}_1\alpha_n \sin(\alpha_n d)\sin[\alpha_n(b-d)] - \sin(\alpha_n b) = \frac{1}{\alpha_n}\frac{\partial Y_{2,n}}{\partial y}(b). \tag{4.5}$$

The eigenvalues $\alpha_n = \sqrt{k^2 - s_n^2}$, $n = 0, 1, 2 \ldots$ are the roots of the following dispersion relation:

$$K(s) = \Omega(\alpha)\Delta(\alpha) - \sin[\alpha(1-b)]\Theta(\alpha) = 0, \quad \text{with } \alpha = \sqrt{k^2 - s^2}, \tag{4.6}$$

where

$$\Delta(\alpha) = i\alpha\mathcal{C}_2 \sin[\alpha(1-b)] - \cos[\alpha(1-b)] \tag{4.7}$$

and

$$\Theta(\alpha) = i\mathcal{C}_1\alpha \sin(\alpha d)\cos[\alpha(b-d)] - \cos(\alpha b). \tag{4.8}$$

From equation (4.6), it is again readily seen that $\alpha_0 = 0$ (corresponding to a plane wave for which $Y_0(y) = 1$) is the first root while the other roots α_n, $n = 1, 2, 3, \ldots$ must be found numerically. The boundary value problem now contains four real parameters, d, b, $\mathcal{C}_1$ and $\mathcal{C}_2$ and there is scope for triple zeros (EP3) of equation (4.6) to arise as well as double zeros (EP2). Before considering the case of a triple zero, it is important to state that the eigenfunctions defined in equations (4.1)–(4.5) satisfy the orthogonality relation, equation (3.3), and it follows that the MM equations obtained in §3 still hold for the case of two wire meshes at non-EP and EP2 conditions provided the appropriate eigenfunctions are substituted. For the case of two wire meshes the additional waveform is given by equation (3.21) with $Y_1(y)$ defined by equations (4.1)–(4.5) and with $\chi(y)$ now defined by

$$\chi(y) = \begin{cases} \chi_1(y), & 0 < y < d, \\ \chi_2(y) + d\dfrac{\partial Y_{2,1}}{\partial y}(y) + (1 + d\alpha_1 \cot(\alpha_1 d))\{Y_{2,1}(y) - Y_{1,1}(y)\}, & d < y < b, \\ \chi_3(y) + \alpha_1 \left\{ \frac{\Omega'(\alpha_1)}{\Omega(\alpha_1)} - (1-b)\cot[\alpha_1(1-b)] \right\} Y_{3,1}(y), & b < y < 1, \end{cases} \tag{4.9}$$

in which

$$\chi_1(y) = y\frac{\partial Y_{1,1}}{\partial y}(y), \quad \chi_2(y) = (y-d)\frac{\partial Y_{2,1}}{\partial y}(y) \quad \text{and} \quad \chi_3(y) = (y-1)\frac{\partial Y_{3,1}}{\partial y}(y).$$

Thus, for two wire meshes, the only case that needs detailed consideration is the case where a triple root occurs (i.e. an EP of order three (EP3)).

Downloaded from http://royalsocietypublishing.org/rspa/article-pdf/doi/10.1098/rspa.2025.0811/6148136/rspa.2025.0811.pdf
by Brunel University user
on 05 July 2026

https://royalsocietypublishing.org/journal/rspa Proc. R. Soc. A 482: 20250811

At an EP3, the function $\chi(y)$ is orthogonal to $Y_1(y)$ and, thus, $Q=0$ (see equation (3.23)). It follows that, the set of functions $Y_n(y)$, $n=0,1,2,\ldots$ together with $\chi(y)$ no longer form a complete set. This implies that, at EP3, a second non-separable waveform exists and, following Lawrie *et al.* [11], this is given by

$$\left.\frac{\partial^2}{\partial s^2}(Y(s,y)\,\mathrm{e}^{\pm \mathrm{i}sx})\right|_{s=s_1} = -\left\{\frac{s_1^2}{\alpha_1^2}\xi(y)+\left(\frac{k^2}{\alpha_1^4}\pm\frac{2\mathrm{i}xs_1}{\alpha_1^2}\right)\chi(y)+x^2Y_1(y)\right\}\mathrm{e}^{\pm \mathrm{i}s_1x}. \tag{4.10}$$

Here, $\xi(y)=-\partial^2_{\alpha\alpha}Y(s,y)|_{\alpha=\alpha_1}$ can be expressed as

$$\xi(y)=\begin{cases} y^2Y_{1,1}(y), & 0<y<d,\\ (y-d)^2Y_{2,1}(y)+(2y-d)dY_{1,1}(y)-d\left(\dfrac{2}{\alpha_1}\cot(\alpha_1 d)-d\right)\{Y_{2,1}(y)-Y_{1,1}(y)\} & \\ \quad -\dfrac{2}{\alpha_1^2}(y-d)(1+\alpha_1\,\mathrm{d}\cot(\alpha_1 d))\{\dfrac{\partial Y_{2,1}}{\partial y}(y)-\dfrac{\partial Y_{1,1}}{\partial y}(y)\}, & d<y<b,\\ \{(y-1)^2-\Upsilon(\alpha_1)\}Y_{3,1}(y)-\dfrac{2}{\alpha_1}(y-1)\dfrac{\partial Y_{2,1}}{\partial y}(y)\Pi(\alpha_1), & b<y<1, \end{cases} \tag{4.11}$$

where

$$\Upsilon(\alpha_1)=\frac{\partial^2_{\alpha\alpha}\Omega(\alpha_1)}{\Omega(\alpha_1)}+(1-b)^2-2(1-b)\cot[\alpha_1(1-b)]\frac{\partial_\alpha\Omega(\alpha_1)}{\Omega(\alpha_1)}+2(1-b)^2\cot^2[\alpha_1(1-b)]$$

and

$$\Pi(\alpha_1)=\frac{\partial_\alpha\Omega(\alpha_1)}{\Omega(\alpha_1)}-(1-b)\cot[\alpha_1(1-b)].$$

Note that $\xi(y)$ satisfies the same boundary conditions as $Y_n(y)$ but a different governing equation: namely $\xi_{yy}+\alpha_1^2\xi=2Y_1+4\chi$. Further, see Lawrie *et al.* [11], $\xi(y)$ is orthogonal to the functions $Y_n(y)$, for $n=0$ and $n=2,3,4,\ldots$, that is,

$$\int_0^1 \xi(y)Y_n(y)\,\mathrm{d}y=R\delta_{1n}. \tag{4.12}$$

Thus, for EP3, two additional waveforms are present and must be included in the expansion for $\bar{\bar{\psi}}_2(x,y)$. The MM procedure is explained in the coming subsections.

(a) Enhanced mode-matching for EP3

The appropriate form for the eigenfunction expansion in the region $x<|\ell|$ is now

$$\begin{aligned}\bar{\bar{\psi}}_2(x,y)=\bar{\psi}_2(x,y)&+\bar{\bar{B}}_1\left\{\frac{s_1^2}{\alpha_1^2}\xi(y)+\left(\frac{k^2}{\alpha_1^4}+\frac{2\mathrm{i}xs_1}{\alpha_1^2}\right)\chi(y)+x^2Y_1(y)\right\}\mathrm{e}^{\mathrm{i}s_1x}\\&+\bar{\bar{C}}_1\left\{\frac{s_1^2}{\alpha_1^2}\xi(y)+\left(\frac{k^2}{\alpha_1^4}-\frac{2\mathrm{i}xs_1}{\alpha_1^2}\right)\chi(y)+x^2Y_1(y)\right\}\mathrm{e}^{-\mathrm{i}s_1x},\end{aligned} \tag{4.13}$$

where $\bar{\psi}_2(x,y)$ is defined in equation (3.24) and the double overbar is used to indicate terms associated with the EP3. The expansion involves addition unknowns $\bar{\bar{B}}_1$, $\bar{\bar{C}}_1$ together with $\bar{B}_1$, $\bar{C}_1$ and B_n and C_n, $n=0,1,2,\ldots$. To find these, the symmetric and anti-symmetric sub-problems are considered.

Downloaded from http://royalsocietypublishing.org/rspa/article-pdf/doi/10.1098/rspa.2025.0811/6148136/rspa.2025.0811.pdf
by Brunel University user
on 05 July 2026

(i) Symmetric sub-problem

For the symmetric case ($\partial_x \bar{\bar{\psi}}_2 = 0$ at $x = 0$), the eigenfunction expansion has the form

$$\bar{\bar{\psi}}_2^s(x,y) = \bar{\psi}_2^s(x,y) + \frac{2\bar{\bar{B}}_1^s}{\sin(s_1\ell)}\left[\frac{s_1^2\cos(s_1x)}{\alpha_1^2}\xi(y) + \left(\frac{k^2\cos(s_1x)}{\alpha_1^4} - \frac{2xs_1\sin(s_1x)}{\alpha_1^2}\right)\chi(y) + x^2\cos(s_1x)Y_1(y)\right], \tag{4.14}$$

where $\bar{\psi}_2^s$ is given in equation (3.24). As for the EP2 case, the expression for the reflected field, as defined by equation (3.6), remains valid and on applying continuity of pressure at the interface ($x = -\ell$), it is found that

$$\begin{aligned} A_m^s = {} & -a_m(-\ell) + B_0^s\frac{4\cos(k\ell)}{\epsilon_m\sin(k\ell)}L_{m0} + \frac{4\bar{B}_1^s}{\epsilon_m}\left[\frac{s_1}{\alpha_1^2}\frac{\cos(s_1\ell)}{\sin(s_1\ell)}M_m + \ell L_{m1}\right] \\ & + \frac{2\bar{\bar{B}}_1^s\cos(s_1\ell)}{\sin(s_1\ell)}\left\{\frac{s_1^2}{\alpha_1^2}N_m + \left(\frac{k^2}{\alpha_1^4} - \frac{2\ell s_1\sin(s_1\ell)}{\alpha_1^2\cos(s_1\ell)}\right)M_m + \ell^2L_{m1}\right\} \\ & + \sum_{n=1}^{\infty}B_n^s\frac{4\cos(s_n\ell)}{\epsilon_m\sin(s_n\ell)}L_{mn}, \end{aligned} \tag{4.15}$$

where

$$N_m = \int_0^1 \xi(y)\cos(m\pi y)\,\mathrm{d}y. \tag{4.16}$$

To apply continuity of normal velocity at the interface, the modal expansions for velocity are equated and, as before, equation (3.12) (with the restriction that $p > 1$) and equation (3.13) hold. Information about $\bar{B}_1^s$ is obtained by multiplying by $Y_1(y)$ (bearing in mind that $P_1 = 0$) and using equation (3.3). Three further coupled equations for B_1^s, $\bar{B}_1^s$ and $\bar{\bar{B}}_1^s$ are obtained by multiplying by $\chi(y)$ (taking into account that $Q = 0$) and using equation (3.23), and multiplying by $\xi(y)$ and using equation (4.12). The latter actions yield

$$\begin{aligned} & 2\begin{pmatrix} 0 & 0 & \frac{s_1^3}{\alpha_1^2}R \\ 0 & \frac{s_1^2}{\alpha_1^2}T & \frac{s_1^3}{\alpha_1^2}U + s_1\left(\frac{k^2}{\alpha_1^4} + \frac{2}{\alpha_1^2}\Xi^+\right)T \\ s_1R & \frac{s_1^2}{\alpha_1^2}U + R\Xi^+ & \frac{s_1^3}{\alpha_1^2}W + s_1\left(\frac{k^2}{\alpha_1^4} + \frac{2}{\alpha_1^2}\Xi^+\right)U + s_1R\Sigma^- \end{pmatrix}\begin{pmatrix} B_1^s \\ \bar{B}_1^s \\ \bar{\bar{B}}_1^s \end{pmatrix} \\ & = \begin{pmatrix} \sum_{n=0}^{N_l-1}a_n'(-\ell)L_{n1} - i\sum_{n=0}^{\infty}A_n^s\eta_nL_{n1} \\ \sum_{n=0}^{N_l-1}a_n'(-\ell)M_n - i\sum_{n=0}^{\infty}A_n^s\eta_nM_n \\ \sum_{n=0}^{N_l-1}a_n'(-\ell)N_n - i\sum_{n=0}^{\infty}A_n^s\eta_nN_n \end{pmatrix}, \end{aligned} \tag{4.17}$$

where Ξ^+ is given in equation (3.28) and

$$U = \int_0^1 \xi(y)\chi(y)\,\mathrm{d}y, \quad \Sigma^- = \ell^2 - \frac{2\ell s_1\cos(s_1\ell)}{\alpha_1^2\sin(s_1\ell)} \quad \text{and} \quad W = \int_0^1 \xi^2(y)\,\mathrm{d}y. \tag{4.18}$$

Downloaded from http://royalsocietypublishing.org/rspa/article-pdf/doi/10.1098/rspa.2025.0811/6148136/rspa.2025.0811.pdf
by Brunel University user
on 05 July 2026

(ii) Anti-symmetric sub-problem

For the anti-symmetric case, the eigenfunction expansion can be expressed as

$$\bar{\bar{\psi}}_2^a(x,y) = \bar{\psi}_2^a(x,y) + \frac{2i\bar{\bar{B}}_1^a}{\cos(s_1\ell)}\left\{\frac{s_1^2\sin(s_1x)}{\alpha_1^2}\xi(y) + \left(\frac{k^2\sin(s_1x)}{\alpha_1^4} + \frac{2xs_1\cos(s_1x)}{\alpha_1^2}\right)\chi(y) + x^2\sin(s_1x)Y_1(y)\right\}, \tag{4.19}$$

where $\bar{\psi}_2^a$ is given in equation (3.29) and the reflected field in equation (3.14).

In this case, continuity of pressure yields

$$\begin{aligned} A_m^a = {} & -a_m(-\ell) - B_0^a\frac{4i\sin(k\ell)}{\epsilon_m\cos(k\ell)}L_{m0} - \frac{4i\bar{B}_1^a}{\epsilon_m}\left[\frac{s_1}{\alpha_1^2}\frac{\sin(s_1\ell)}{\cos(s_1\ell)}M_m - \ell L_{m1}\right] \\ & - \frac{2i\bar{\bar{B}}_1^a\sin(s_1\ell)}{\cos(s_1\ell)}\left\{\frac{s_1^2}{\alpha_1^2}N_m + \left(\frac{k^2}{\alpha_1^4} + \frac{2\ell s_1\cos(s_1\ell)}{\alpha_1^2\sin(s_1\ell)}\right)M_m + \ell^2L_{m1}\right\} \\ & - \sum_{n=1}^{\infty}B_n^a\frac{4i\sin(s_n\ell)}{\epsilon_m\cos(s_n\ell)}L_{mn}, \end{aligned} \tag{4.20}$$

and, as before, the continuity of normal velocity at the interface yields equation (3.17) (with the restriction that $p > 1$) and equation (3.18). For B_1^a, $\bar{B}_1^a$, $\bar{\bar{B}}_1^a$ additional equations are obtained using equations (3.3), (3.23) and (4.12), yielding

$$\begin{aligned} & 2i\begin{pmatrix} 0 & 0 & \frac{s_1^3}{\alpha_1^2}R \\ 0 & \frac{s_1^2}{\alpha_1^2}T & \frac{s_1^3}{\alpha_1^2}U + s_1\left(\frac{k^2}{\alpha_1^4} + \frac{2}{\alpha_1^2}\Xi^-\right)T \\ s_1R & \frac{s_1^2}{\alpha_1^2}U - s_1R\Xi^- & \frac{s_1^3}{\alpha_1^2}W + s_1\left(\frac{k^2}{\alpha_1^4} + \frac{2}{\alpha_1^2}\Xi^-\right)U - s_1R\Sigma^+ \end{pmatrix}\begin{pmatrix} B_1^a \\ \bar{B}_1^a \\ \bar{\bar{B}}_1^a \end{pmatrix} \\ & = \begin{pmatrix} \sum_{n=0}^{N_I-1}a_n'(-\ell)L_{n1} - i\sum_{n=0}^{\infty}A_n^a\eta_nL_{n1} \\ \sum_{n=0}^{N_I-1}a_n'(-\ell)M_n - i\sum_{n=0}^{\infty}A_n^a\eta_nM_n \\ \sum_{n=0}^{N_I-1}a_n'(-\ell)N_n - i\sum_{n=0}^{\infty}A_n^a\eta_nN_n \end{pmatrix}, \end{aligned} \tag{4.21}$$

where Ξ^- is given in equation (3.32) and

$$\Sigma^+ = \ell^2 + \frac{2\ell s_1\sin(s_1\ell)}{\alpha_1^2\cos(s_1\ell)}.$$

Once the symmetric and anti-symmetric amplitudes are known, the amplitudes for the full problem can be obtained using equations (3.19), (3.20) and (3.33) together with

$$\bar{\bar{B}}_1 = \frac{\bar{\bar{B}}_1^s}{2\sin(s_1\ell)} + \frac{\bar{\bar{B}}_1^a}{2\cos(s_1\ell)} \quad \text{and} \quad \bar{\bar{C}}_1 = \frac{\bar{\bar{B}}_1^s}{2\sin(s_1\ell)} - \frac{\bar{\bar{B}}_1^a}{2\cos(s_1\ell)}. \tag{4.22}$$

Downloaded from http://royalsocietypublishing.org/rspa/article-pdf/doi/10.1098/rspa.2025.0811/6148136/rspa.2025.0811.pdf
by Brunel University user
on 05 July 2026

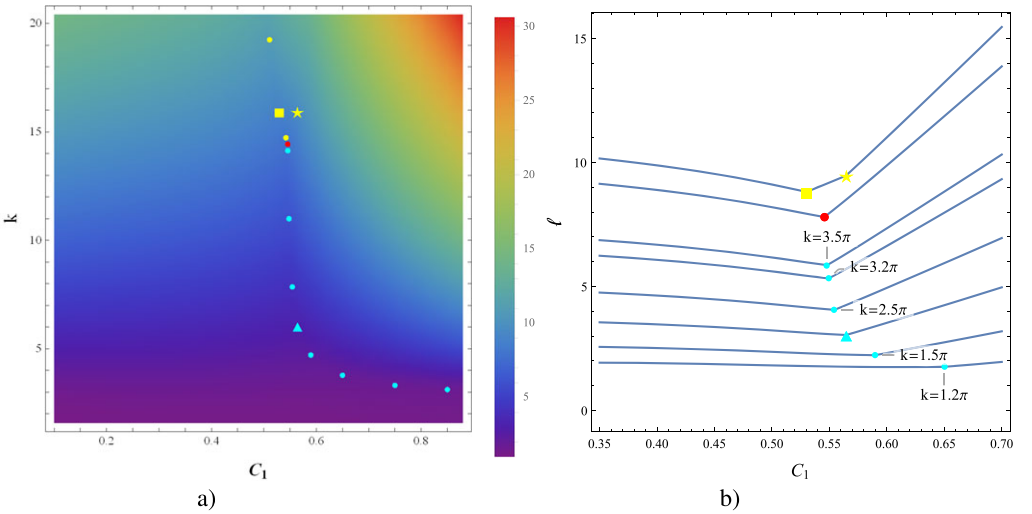

Figure 5. In both (a) and (b), the light blue markers show the co-ordinates at which the attenuation of the EP2 mode (for the relevant value of $\mathcal{C}_1$) coincides with that of HM1, the yellow markers show the co-ordinates at which the attenuation of the EP2 mode coincides with that of HM2. The red point indicates where the attenuation of the EP2 mode coincides with that of both HM1 and HM2. (a) Map of $\ell = -\ln(0.05)/\Im(s_L)$ (where s_L is the least attenuated non-plane wave) at EP2 plotted against $\mathcal{C}_1$ and k with $b = 1 - d$. In the region of the map lying to the left of the markers the EP2 mode is the least attenuated mode. (b) Plots of ℓ against $\mathcal{C}_1$ at EP2 for a range of values of k with $b = 1 - d$. It is clear that, for all selected values of k, the best attenuation (equivalently the smallest value of ℓ) occurs when the attenuation of the EP2 mode merges with that of a higher mode.

(iii) Results for exceptional points of order two

As for the case of one wire mesh, with the exception of $\alpha_0 = 0$, the roots, α_n, $n = 1, 2, 3, \ldots$, of the characteristic equation, equation (4.6), are complex and there exist critical values of the real parameters b, d, $\mathcal{C}_1$ and $\mathcal{C}_2$ that give rise to EPs. The increased number of parameters (four as opposed to two in §3) allows for the possibility of many more EPs to exist but locating these is both algebraically and numerically more complicated. However, provided $\mathcal{C}_1$ is specified and b is expressed as a function of d (for example, $b = 1 - d$), the process described for one wire mesh can be used to find EP2s. On treating $\mathcal{C}_2$ as a function of α, equation (4.6) gives

$$\mathcal{C}_2(\alpha) = -\frac{i(\Theta(\alpha)\sin[\alpha(1-b)] + \Omega(\alpha)\cos[\alpha(1-b)])}{\alpha\Omega(\alpha)\sin[\alpha(1-b)]}. \tag{4.23}$$

Note that $\partial_s K(s) = -\frac{s}{\alpha}\partial_\alpha K(s)$, hence it is necessary to solve

$$\begin{aligned}\partial_\alpha K(s) = {} & \partial_\alpha \Omega(\alpha)\Delta(\alpha) + \Omega(\alpha)\partial_\alpha \Delta(\alpha) - \sin[\alpha(1-b)]\partial_\alpha \Theta(\alpha) \\ & - (1-b)\cos[\alpha(1-b)]\Theta(\alpha) = 0,\end{aligned} \tag{4.24}$$

with $\mathcal{C}_2(\alpha)$ given by equation (4.23). As $\mathcal{C}_2(\alpha_1)$ is required to be real and positive, EP2s can be found by using the bisection method to determine the value of d for which the first root of equation (4.24) satisfies $\Im(\mathcal{C}_2) = 0$. Having found the critical values of d and $\mathcal{C}_2$, the roots α_n, $n = 1, 2, 3, \ldots$ can be found by solving $K(s) = 0$, where $K(s)$ is given by equation (4.6).

For the case $b = 1 - d$, $0 < \mathcal{C}_1 < 1$, there is a continuum of EP2s each corresponding to the coalescence of α_1 and α_2. While it might be expected that all such EPs, provided they do correspond to the least attenuated non-plane wave, perform better in terms of mode filtering than nearby non-EP configurations, the question naturally arises as to which performs the best. To explore this question figure 5a maps $\ell = -\ln(0.05)/\Im(s_L)$ (where s_L is the least attenuated non-plane wave) against k and $\mathcal{C}_1$. The dark blue areas of the map show the shortest values of ℓ and

Downloaded from http://royalsocietypublishing.org/rspa/article-pdf/doi/10.1098/rspa.2025.0811/6148136/rspa.2025.0811.pdf
by Brunel University user
on 05 July 2026

hence the best choice of parameters to achieve optimal attenuation. As mentioned at the end of §3, the EP2 mode may be the least attenuated non-plane wave only for a range of k. As $k \to 0$ the EP mode is always the least attenuated; however, for the frequency range considered here and for $\mathcal{C}_1 > 0.5$, as k increases the attenuation of the EP mode decreases more slowly than one or more higher mode until the EP mode is no longer the least attenuated. Further, it depends on the value of $\mathcal{C}_1$ as to which of the higher-order modes take over as the least attenuated.

For the sake of clarity, it is worth reiterating that, for duct configurations in which the plane wave is the only mode unaffected by the presence of the wire mesh(es), all other modes propagating in the middle section of the duct are attenuated. The first four such modes will be referred to in terms of their attenuation as $k \to 0$. The EP mode is the least attenuated non-plane wave mode as $k \to 0$ and the next three least attenuated modes (as $k \to 0$) will be referred to as higher-order modes 1–3 (HM1–HM3). In figure 5a,b, the light blue markers show the co-ordinates at which the attenuation of the EP2 mode (for the relevant value of $\mathcal{C}_1$) coincides with that of HM1 (which thus becomes the new least attenuated mode as k increases for fixed $\mathcal{C}_1$). The yellow markers show the co-ordinates at which the attenuation of the EP2 mode coincides with HM2 (thus this is the new least attenuated mode as k increases for fixed $\mathcal{C}_1$). It follows that, in figure 5a in the region of the map lying to the left-hand side of the markers the EP2 mode is the least attenuated non-plane wave but in the region to the right-hand side of the markers it is not. It is clear that, as k increases, there is a near vertical shadow in the map which encompasses the markers. For k greater than approximately 1.5π, this region offers the best values of ℓ (and hence the best choice of parameters) for a given frequency. Note that, for $k = 15.998$, there are two yellow markers. The square corresponds to $\mathcal{C}_1 = 0.53$ and indicates the point at which the EP mode has the same attenuation as HM2. The star corresponds to $\mathcal{C}_1 = 0.5646$ and indicates the point at which the least attenuated mode (which is not the EP mode) has the same attenuation as HM2. For $k = 6.118$ and $\mathcal{C}_1 = 0.5646$, the blue triangle indicates where the EP mode has the same attenuation as HM1. Figure 5b shows plots of ℓ against $\mathcal{C}_1$ at EP2 for a range of values of k with $b = 1 - d$. Each curve is a horizontal cross-section through the map shown in figure 5a at the specified value of k. It is clear that, for all selected values of k, the smallest value of ℓ occurs when the attenuation of the EP2 mode merges with that of a higher mode. Note that it is the attenuations that merge and this is not the same as EP3 conditions where three values of α merge. Also, for each value of k, the best attenuation is given by a different set of EP parameters. In the next two figures, the square, star and triangle symbols indicate the same points as in figure 5.

Figure 6 shows the attenuation, $\Im(s_n)$, $n = 1, 2, 3, 4$ for the EP mode (labelled as EP) and those modes which are the next three higher-order modes as $k \to 0$ (labelled as HM1, HM2, HM3). In figure 6a, $\mathcal{C}_1 = 0.53$ and it is clear the attenuation of the EP mode and that of HM2 are the same at $k = 15.998$, as k increases beyond this value HM2 is the least attenuated mode. Although showing attenuation as opposed to ℓ, this figure is equivalent to a vertical cross-section through $\mathcal{C}_1 = 0.53$ in figure 5 passing through the yellow square. In figure 6b, $\mathcal{C}_1 = 0.5646$ and it is clear that the attenuation of the EP mode and that of HM1 are the same at $k = 6.118$. For $6.118 < k < 15.998$, HM1 is the least attenuated mode while for $k > 15.998$, HM2 is the least attenuated mode. This figure is equivalent to a vertical cross-section through $\mathcal{C}_1 = 0.5646$ in figure 5 passing through the blue triangle and the yellow star.

There is one marker in figure 5 that has not as yet been discussed. The red marker, located at $\mathcal{C}_1 = 0.545\,57$ and $k = 14.4341$, indicates the point where the attenuation of the EP2 mode converges with that of HM1 and HM2. For $k > 14.4341$, the attenuation of the EP2 mode remains very close to that of HM1, whilst HM2 is the least attenuated mode. This is shown in figure 7a in which the red marker of figure 5 is indicated by a circle. Figure 7b shows the least attenuated modes for a selection of values of $\mathcal{C}_1$. The red curves (dashed and solid) are the EP2 modes for the respective values of $\mathcal{C}_1$, whereas the blue dashed curves are HM1 modes. Further, on studying figure 5b it is clear that, while for each value of k the best attenuation is given by a different set of EP parameters, the most attenuated EP modes for $2.5\pi \leq k \leq 14.4341$ are given by values of $\mathcal{C}_1$ lying in quite a small range, that is, $0.545\,57 < \mathcal{C}_1 < 0.554\,248$.

Downloaded from http://royalsocietypublishing.org/rspa/article-pdf/doi/10.1098/rspa.2025.0811/6148136/rspa.2025.0811.pdf
by Brunel University user
on 05 July 2026

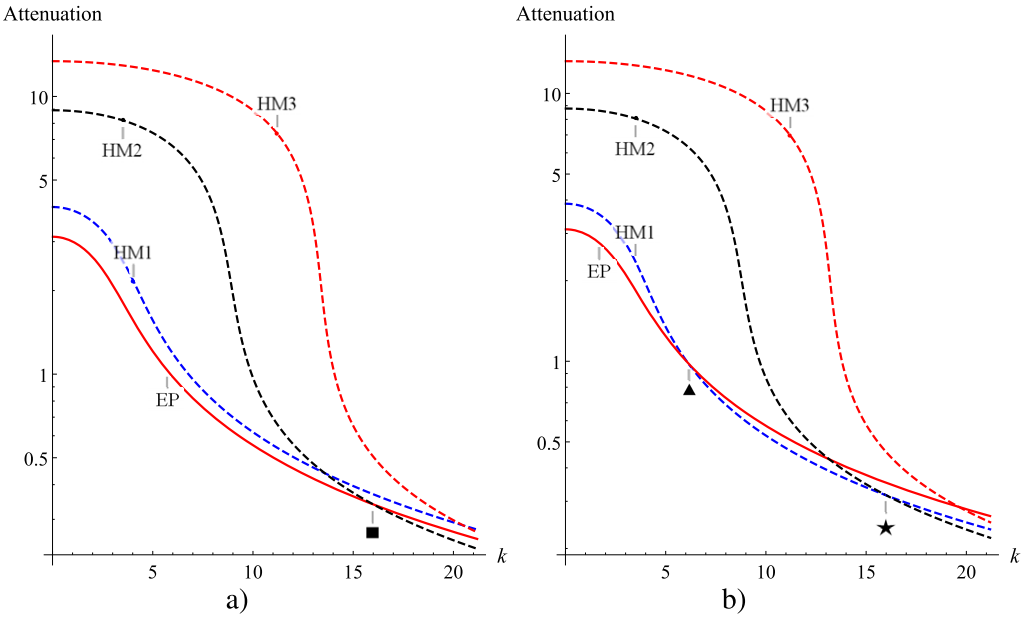

Figure 6. Attenuation curves for the EP mode and the next three higher modes for (a) $\mathcal{C}_1 = 0.53$ and (b) $\mathcal{C}_1 = 0.5646$.

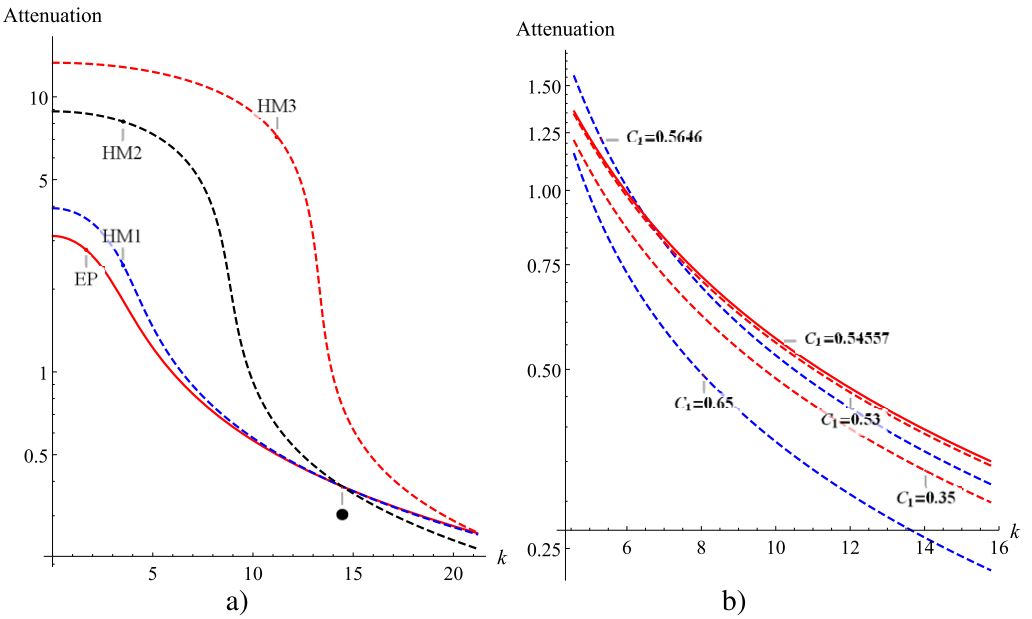

Figure 7. (a) Attenuation curves for the EP mode and the next three higher modes for $\mathcal{C}_1 = 0.545\,57$; (b) the least attenuated modes for $5 < k < 15$ at a selection of $\mathcal{C}_1$. For the values of $\mathcal{C}_1$ considered, the solid red curve ($\mathcal{C}_1 = 0.545\,57$) is the least attenuated (non-plane wave) mode with the greatest attenuation.

The features discussed in relation to figures 5–7 suggest that the EP corresponding to $\mathcal{C}_1 = 0.54557$ may produce a good filtering effect for a range of k ($6.118 < k < 14.4341$) and, going forward, this EP is referred to as the optimum EP2 even though this is strictly true only for $k = 14.4341$. In figure 8 the absolute value of the velocity potential is plotted for $k = 14.4341$,

Downloaded from http://royalsocietypublishing.org/rspa/article-pdf/doi/10.1098/rspa.2025.0811/6148136/rspa.2025.0811.pdf
by Brunel University user
on 05 July 2026

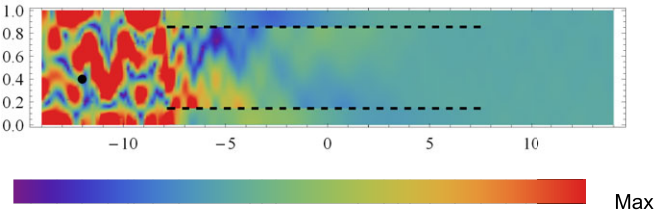

Figure 8. Absolute value of the velocity potential for two wire meshes (length 2ℓ) at EP2 conditions: $k = 14.4341$, $\ell = 7.8$; $C_1 = 0.54557$, $C_2 = 0.833135$, $d = 0.145\,171$. The dashed lines and black point indicate the wire meshes and source, respectively.

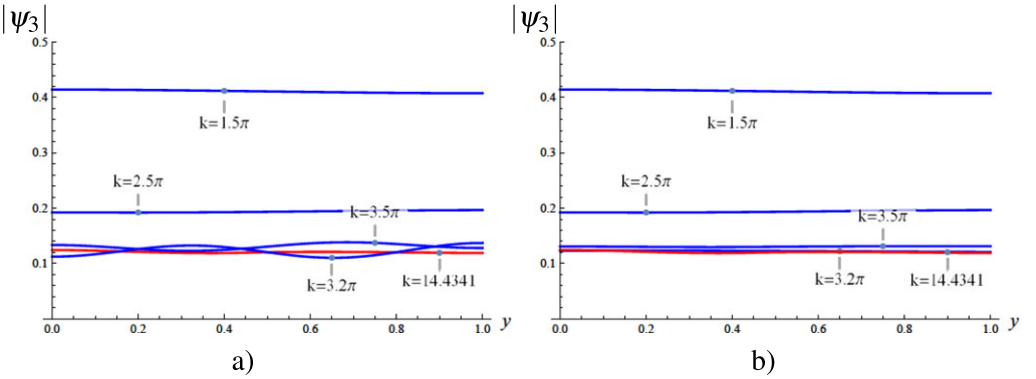

Figure 9. Absolute value of the velocity potential at $x = \ell + 1$ against y (two wire meshes) (a) at EP2 with $C_1 = 0.545\,57$, $C_2 = 0.833\,135$, $d = 0.145\,171$. In (a) $\ell = -\ln(0.05)/\Im(s_1)$ and thus, in order of increasing k, $\ell = 2.28$, 4.09, 5.34, 5.88 and 7.8. In (b), the values of ℓ are as for (a) except for $k = 3.2\pi$ and 3.5π where ℓ is given by $|e^{is_1\ell}| = 0.05$ so, in order of increasing k, $\ell = 2.28$, 4.09, 7.09, 7.9 and 7.8.

$C_1 = 0.54557$, $C_2 = 0.833\,135$, $d = 0.145\,171$. The dashed lines indicate the wire meshs which are of length 2ℓ with $\ell = -\ln(0.05)/\Im(s_1) = 7.8$. The uniformity of colour for $x > \ell$ suggests that only the plane wave propagates; however, to verify the quality of filtering it is useful to consider the profile of the field in this region for a range of values of k. This is shown in figure 9a. It is clear that filtering is effective at $k = 14.4341$ and also at lower frequencies $k = 1.5\pi$ and 2.5π (for which $\ell = 2.28$ and 4.09, respectively). However, it is not as effective at $k = 3.2\pi$ or $k = 3.5\pi$ ($\ell = 5.34$ and $\ell = 5.88$, respectively) or indeed for any values of k the interval $3.1\pi < k < 4.2\pi$. This is thought to be due to coupling between the EP waveform (which grows as x) and the higher-order rigid duct modes and is, to some extent, resolved by increasing ℓ such that $\sqrt{\ell}\,\mathrm{e}^{\mathrm{i}s_1\ell} = 0.05$. Figure 9b shows the same profiles but in this case $\ell = 7.09$ and $\ell = 7.9$ for $k = 3.2\pi$ and 3.5π, respectively, whilst ℓ is unchanged for other values of k. It is clear that the quality of filtering has been improved. Further discussion regarding the quality of filtering for both one wire mesh and two is presented in §5.

(iv) Results for exceptional points of order three

The EP3s of interest correspond to the coalescence of the first three higher modes, that is, $K(s_1) = K'(s_1) = K''(s_1) = 0$, where $K''(s) = -\frac{k^2}{\alpha^3}\partial_\alpha K(s) + \frac{s^2}{\alpha^2}\partial^2_{\alpha\alpha}K(s)$ with $\partial_\alpha K(s)$ given by equation (4.24) and

$$\partial^2_{\alpha\alpha}K(s) = \partial^2_{\alpha\alpha}\Omega(\alpha)\Delta(\alpha) + 2\partial_\alpha\Omega'(\alpha)\partial_\alpha\Delta(\alpha) + \Omega(\alpha)\partial^2_{\alpha\alpha}\Delta(\alpha) + \{(1-b)^2\Theta(\alpha) - \partial^2_{\alpha\alpha}\Theta(\alpha)\}\sin[\alpha(1-b)] - 2((1-b)\cos[\alpha(1-b)]\partial_\alpha\Theta(\alpha). \quad (4.25)$$

Downloaded from http://royalsocietypublishing.org/rspa/article-pdf/doi/10.1098/rspa.2025.0811/6148136/rspa.2025.0811.pdf
by Brunel University user
on 05 July 2026

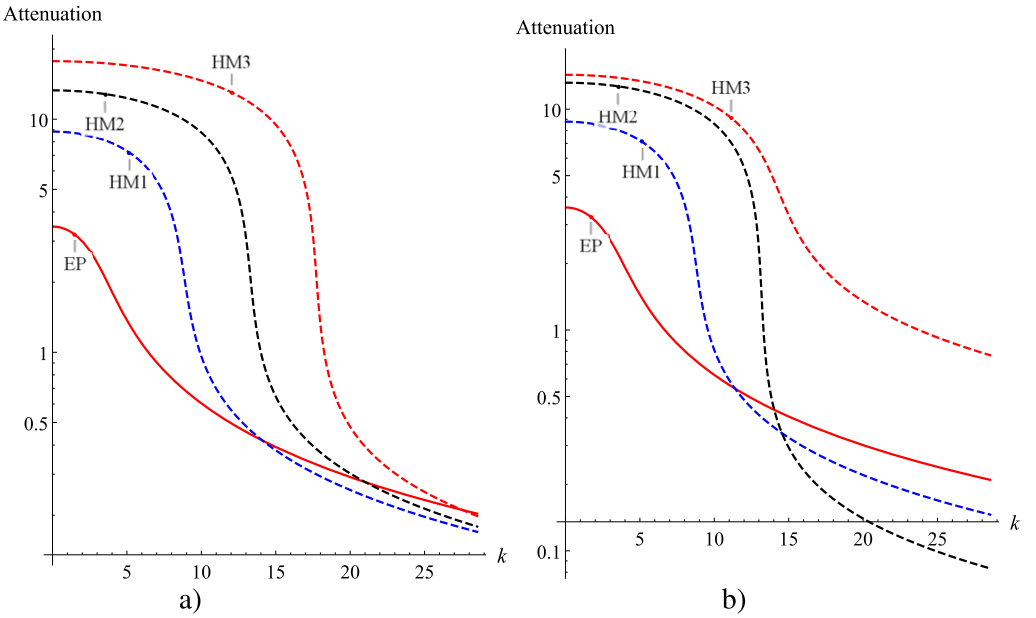

Figure 10. Attenuation curves for the EP mode and the first three higher modes for EP3s of table 1: (a) EP3 of first row and (b) EP3 of second row.

Table 1. Numerical values (to six digit accuracy) of the wire-mesh parameters giving rise to the EP3s and the optimum EP2 considered in §4a(iii).

	$\mathcal{C}_1$	$\mathcal{C}_2$	b	d	transverse wavenumber
EP3	0.542 509	0.744 667	0.843 693	0.133 414	$\bar{\bar{\alpha}}_1 = 3.462\,543 - 1.665\,488i$
EP3	0.351 734	1.473 222	0.943 613	0.723 013	$\bar{\bar{\alpha}}_1 = 3.587\,827 - 1.657\,148i$
EP2	0.545 57	0.833 135	0.854 829	0.145 171	$\bar{\alpha}_1 = 3.119\,575 - 1.748\,755i$

Determining the critical values of the constants $\mathcal{C}_1$, $\mathcal{C}_2$, d and b (with $\mathcal{C}_1$ and $\mathcal{C}_2$ real and $d < b$) for an EP3 is non-trivial. However, two have been located[1] and are listed in table 1 together with the optimum EP2 (discussed above) for comparison.

Figure 10 shows the attenuation, $\Im(s_L)$, for the EP3 mode (labelled as EP) and those modes which are the next three higher-order modes as $k \to 0$ (indicated by HM1, HM2, HM3) for both EP3s of table 1. It is clear that there is a wider range of k for which the EP3 of the first row of table 1 is the least attenuated mode. For this reason, attention is henceforth restricted to this EP3, although we note that HM1 and the EP mode have the same attenuation at $k = 14.1018$. Thus, at $k = 14.4341$, the HM1 mode is, in fact, the least attenuated non-plane wave but the two modal attenuations are very close. Note too that the parameter values for this EP3 are, in fact, quite close to those for the optimum EP2, in particular, $b \approx 1 - d$.

To assess the quality of filtering at EP3 conditions, the profile of the field in the region $x > \ell$ for a range of values of k is considered. This is shown in figure 11a. It is clear that for $\ell = -\ln(0.05)/\Im(s_1)$ filtering is not very effective, even for $k = 1.5\pi$, and this is thought to be due to coupling between the additional EP2 and, in particular, EP3 waveforms (which grow as x and x^2, respectively, see equation (4.13)) and the higher-order rigid duct modes. Filtering is particularly poor for $k = 3.2\pi$ and $k = 3.5\pi$. The quality of filtering can be improved by increasing ℓ. Figure 11b shows the same

[1]The authors are grateful to Dr Benoit Nennig (BN) for his assistance in this matter. The code developed and used by BN for locating EPs can be found in [31].

Downloaded from http://royalsocietypublishing.org/rspa/article-pdf/doi/10.1098/rspa.2025.0811/6148136/rspa.2025.0811.pdf
by Brunel University user
on 05 July 2026

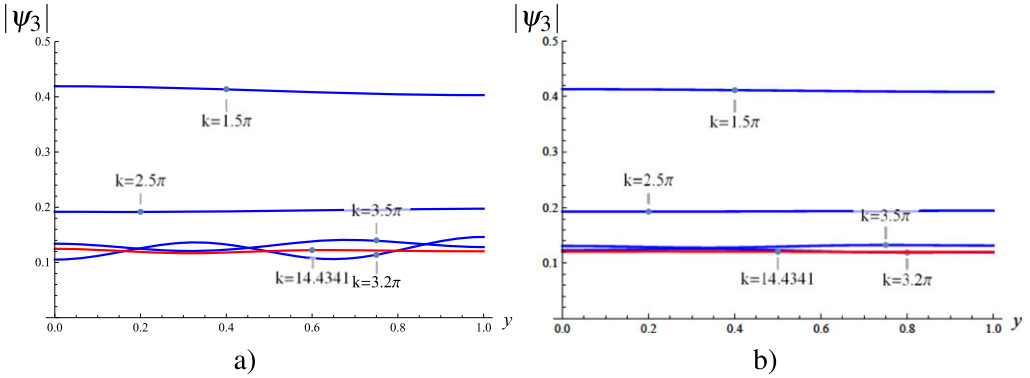

Figure 11. Absolute value of the velocity potential at $x = \ell + 1$ against y (two wire meshes) at EP3 conditions with (a) $\mathcal{C}_1 = 0.542\,509$, $\mathcal{C}_2 = 0.744\,667$, $d = 0.133\,414$ and $b = 0.843\,693$. In (a) $\ell = -\ln(0.05)/\Im(s_1)$ and thus, in order of increasing k, $\ell = 2.02, 3.79, 4.99, 5.498$ and 7.334. In (b), ℓ is given by $|\sqrt{\ell}e^{js_1\ell}| = 0.05$ so, in order of increasing k, $\ell = 2.31, 4.77, 6.55, 7.33$ and 10.17.

profiles for increased values of ℓ (see the figure captions for details). It is clear that filtering quality has been improved; however, the values of ℓ required to do this are close to those required for the optimum EP2 considered above. Further at $k = 3.5\pi$ even with $\ell = 7.2$ (cf. $\ell = 7.9$ for EP2, see figure 9b) the quality of filtering is not excellent since the undulation of the curve is easily visible indicating that the field for $x > \ell$ does not comprise a pure plane wave. This situation can be improved by further increasing ℓ; however, this will bring the value of ℓ close to or even greater than that for EP2 indicating that, for this value of k, EP3 may offer little advantage over the optimum EP2 considered above. The latter point is discussed more fully in the next section.

5. Discussion

It is useful to quantify how successful the filtering is for each configuration considered in §§3 and 4. For configurations in which the plane wave is the only incident wave that is unaffected by the wire mesh(es), it is expected that $\psi_3(x, y) \approx D_0\, \mathrm{e}^{\mathrm{i}\eta_0(x-\ell)}$, $x > \ell$. Thus, a measure of the percentage deviation of the velocity potential from the expected solution, at $x = \ell + 1$, can be constructed according to

$$Dev = 100 \left| \frac{\int_0^1 |D_0\, \mathrm{e}^{\mathrm{i}\eta_0} - \psi_3(\ell + 1, y)| dy}{|D_0\, \mathrm{e}^{\mathrm{i}\eta_0}|} \right|. \tag{5.1}$$

Clearly, total filtering has been achieved only if the deviation is zero. Figure 12 shows the deviation plotted against ℓ at $k = 1.5\pi, 2.5\pi$ and 3.5π for each filtering configuration considered in this paper.

On considering figure 12a–c, it is clear that filtering performance is improved by using two wire meshes (red curves) rather than one (blue curves). However, for the case of one wire mesh, figure 12a,b demonstrates that, at $k = 1.5\pi$ and 2.5π the non-EP configuration performs as well as or better than the EP configuration, although for $k = 3.5\pi$ the situation is reversed with the EP out performing the non-EP. This result was not expected and conflicts with the usually held tenet that optimum attenuation provides the best conditions for modal decay. A second unexpected observation is that, for two wire meshes, the optimum EP2 ($\mathcal{C}_1 = 0.54557$, see figure 7a) performs as well as or better than the EP3 at all values of k considered. However, it is impossible to confirm whether or not there is a non-EP configuration, or another EP2 with $b \neq 1 - d$, which out performs this.

All the results presented in this paper have been for a source fixed at $(-12, 0.4)$ and with the wire mesh length varying but centred on the origin. Thus, for each configuration, the distance

Downloaded from http://royalsocietypublishing.org/rspa/article-pdf/doi/10.1098/rspa.2025.0811/6148136/rspa.2025.0811.pdf
by Brunel University user
on 05 July 2026

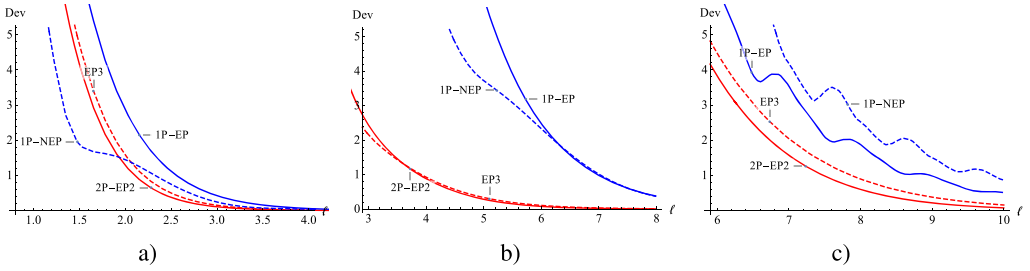

Figure 12. Deviation of the velocity potential from the expected solution against ℓ at (a) $k = 1.5\pi$, (b) $k = 2.5\pi$ and (c) $k = 3.5\pi$. Each figure shows the percentage deviation for the four filtering configurations considered in §§3 and 4, that is: one wire mesh with no EP (1P-NEP, dashed blue curve) and with EP (1P-EP, blue curve) (parameters given in figures 2 and 3), two wire meshes at EP2 (2P-EP2, red curve) and EP3 (EP3, dashed red curve) (parameters given in figures 8 and 11).

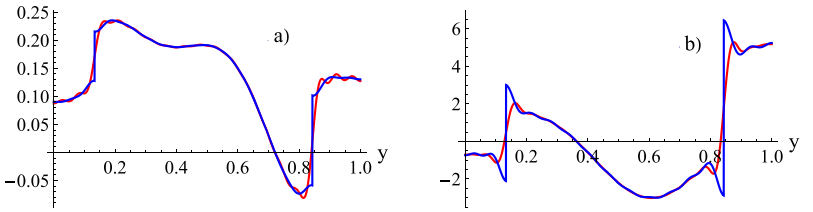

Figure 13. Real parts of (a) pressure and (b) normal velocity for EP3 conditions with $k = 3.5\pi$ at the matching interface $x = -\ell$ with $\ell = 7.55$ and N=40. The red curves correspond to $\psi_1(-\ell, y)$ and $\psi_{1x}(-\ell, y)$ while the blue curves correspond to $\psi_2(-\ell, y)$ and $\psi_{2x}(-\ell, y)$. Note that $\psi_{1x}(-\ell, y)$ is calculated using the Lancos filter, see [33].

between the source and the edge of the wire mesh(es) varies, so the wire mesh(es) are not subject to exactly the same forcing. With this in mind, a second set of 'deviations' was explored with $(x_0, y_0) = (-\ell - 2, 0.4)$ so that the distance between the source and the edge of the wire mesh was constant. Although the results differed quantitatively from those of figure 12, they were qualitatively the same and the same comments applied. This is perhaps not unexpected since, by moving the source in this manner, all that is affected is the phase of each individual incident mode as it impinges on the wire mesh(es); the absorbing capacity of the wire mesh(es) is unaffected.

Further, all the results in this paper have been presented on the assumption that the enhanced MM method is valid and converges to the correct solution. Note that the energy balance is a poor means of checking the validity or convergence of MM methods. For the non-dissipative case (corresponding to $\mathcal{C}_1$ and $\mathcal{C}_2$ both being imaginary), the power balance is automatically satisfied regardless of the truncation of the system [32] and thus only provides a check on the algebraic integrity of the solution. For example, it holds for very low truncations and even when the system is truncated at a value which is less than the number of modes propagating in the incident field. The situation is better for the dissipative case but the power still appears to balance before the solution has adequately converged. The usual approach to validating MM methods is, therefore, to plot the normal velocity and pressure at each matching interface. Note that, at the matching interface, the pressure should match to a high degree of accuracy, the mean normal velocity is conserved but the velocity itself is subject to Gibb's phenomena owing to the singular nature of this quantity.

Figure 13 shows the real parts of pressure and normal velocity at $x = -\ell^{\pm}$ for the EP3 parameters given in the first row of table 1 with $\ell = 7.55$ and $N = 40$. It is clear that the matching conditions are satisfied (except in the vicinities of $y = d$ and $y = b$ where the fields are discontinuous, see equation (2.5) and (2.6)). (The imaginary parts of pressure and normal velocity show the same levels of agreement as the real parts.) The agreement between the pressures and

Downloaded from http://royalsocietypublishing.org/rspa/article-pdf/doi/10.1098/rspa.2025.0811/6148136/rspa.2025.0811.pdf
by Brunel University user
on 05 July 2026

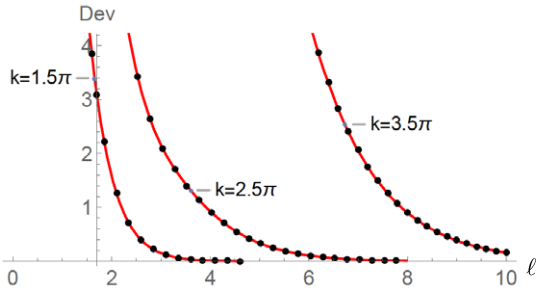

Figure 14. Deviation of the absolute velocity potential at EP3 conditions from the expected solution against ℓ for $k = 1.5\pi$, 2.5π and 3.5π. The solid curves are identical to the dashed red curves (EP3) of figure 12 and are calculated using $N = 40$ whereas for the black points $N = 60$.

normal velocities at $x = -\ell$ can be improved by increasing N albeit at increased computational cost. Note that as ℓ increases the matching conditions at $x = \ell$ are better satisfied owing to the filtering effect of the wire meshes which ensure that the field is near planar. For comparison, figure 14 shows the deviation from the expected solution, as defined by equation (5.1), for EP3 conditions at three different values of k. The solid curves (which are identical to the dashed red curves (EP3) of figure 12) are calculated using $N = 40$ whereas for the black points $N = 60$. The agreement between the two truncations is good with each value agreeing to two decimal places. Figures 13 and 14 demonstrate that the enhanced MM procedure has yielded the correct solution with a good level of accuracy for $N = 40$, although undoubtedly increasing the truncation will further improve accuracy.

To conclude, it has been shown that the enhanced MM method developed by Lawrie *et al.* [11] can be successfully implemented for three-part ducts at EP conditions. It has been demonstrated that, for one wire mesh, at lower values of k, the non-EP configuration considered herein performs better than the EP configuration, although as k increases this is not the case. Thus, for $k = 1.5\pi$ and $\ell = 3.5$ (the values chosen by Kuznetsova *et al.* [26]), it is the non-EP configuration that appears to give the best filtering performance, although the difference between the four configurations is small (see figure 12). The effect of introducing a second wire mesh has been investigated and it has been shown that this can significantly improve mode filtering. In particular, it has been shown that for $b = 1 - d$, $0 < \mathcal{C}_1 < 1$, there is a continuum of EP2s each corresponding to the coalescence of α_1 and α_2.[2] For any given k, only one such EP2 has the best attenuation and is thus the best choice for filtering. This is the EP2 for which the attenuation coincides with that for one of the higher-order modes—an effect that should not be confused with EP3 conditions. For two wire meshes with $k = 14.4341$, optimum attenuation is given by the EP2 corresponding to $\mathcal{C}_1 = 0.54557$. In fact, this configuration gives optimum or near optimum attenuation for $6.118 < k < 14.4341$. Further, the filtering performance of this configuration out performs the one wire-mesh case and performs as well as or better than two wire meshes at EP3 (see figure 12) for the values of k considered herein. Thus, although there has been much recent interest in taking advantage of the concept of optimum attenuation to improve the efficiency of sound absorbing devices, e.g. [18–20], the key findings of this paper suggest that caution is required particularly at EP3 conditions. The algebraic growth of the non-separable additional waveforms (the generalized eigenfunctions) which arise at EP3 conditions can offset, at least in part, the improved attenuation.

[2]Note that $b = 1 - d$ is not the only situation whereby a continuum of EP2s exists. For example, the choices $b = 1 - 2d$ and $b = 1 - d/2$ also generate a continuum of EP2s. However, precursory investigations suggest that, while these choices show similar features to those observed for $b = 1 - d$, the attenuations achieved are not as good. Naturally, however, there are many other choices which have not been considered.

Downloaded from http://royalsocietypublishing.org/rspa/article-pdf/doi/10.1098/rspa.2025.0811/6148136/rspa.2025.0811.pdf
by Brunel University user
on 05 July 2026

Data accessibility. This article has no additional data.

Declaration of AI use. We have not used AI-assisted technologies in creating this article.

Authors' contributions. J.B.L.: conceptualization, formal analysis, investigation, methodology, writing—original draft, writing—review and editing; M.A.: conceptualization, formal analysis, writing—original draft, writing—review and editing.

Both authors gave final approval for publication and agreed to be held accountable for the work performed therein.

Conflict of interest declaration. We declare we have no competing interests..

Funding. M.A. was supported by The Gulf University for Science and Technology through internal Seed grant no. 145.

Acknowledgements. We thank Dr Benoit Nennig for assistance in locating the parameter values for EP3 conditions and for his insightful comments on the paper. J.B.L. would like to acknowledge the Isaac Newton Institute for Mathematical Sciences, Cambridge, for support and hospitality during the programme Mathematical theory and applications of multiple wave scattering, where a talk by one of the participants inspired the work for this paper. The programme was supported by EPSRC grant no. EP/R014604/1.

Appendix A. Pointwise convergence at an exceptional point

In the absence of an EP, the set of eigenfunctions $Y_n(y)$, $n=1,2,3,\ldots$ are complete and pointwise convergence of the modal expansions to the functions ψ_j, $j=1,2,3$ (and their x derivatives) is assured. However, at an EP, $Y_1(y)$ is self orthogonal and additional function(s) (often referred to as generalized eigenfunctions [6]) must be added to the set in order to ensure pointwise convergence. In §3, the function $\chi(y)$ was introduced for the EP2 case and in §4, a further function, $\xi(y)$, was added for the EP3 case. Here, it is demonstrated that these are appropriate choices.

Consider first the non-EP case. Lawrie *et al.* [11] derived the following expression:

$$D_1(v,y)=\sum_{n=0}^{\infty}\frac{Y_n(v)Y_n(y)}{P_n}=\delta(v-y)-\delta(v+y)+\delta(y+v-2),\quad 0<v,y\le 1, \tag{A 1}$$

where $\delta()$ is the Dirac delta function. Although this was derived for a different set of duct modes, the result holds true for this problem and confirms pointwise convergence in the case of no EP. At EP2, the result is altered slightly. As in the main body of the paper, attention will be restricted to the case where the EP occurs at $\alpha=\alpha_1$ which implies that $P_1=0$. The appropriate result becomes

$$\begin{aligned}D_2(v,y)&=\sum_{n=2}^{\infty}\frac{Y_n(v)Y_n(y)}{P_n}+\frac{\chi(v)Y_1(y)+Y_1(v)\chi(y)}{Q}-\frac{T}{Q^2}Y_1(v)Y_1(y)+\frac{Y_0(v)Y_0(y)}{P_0}\\&=\delta(v-y)-\delta(v+y)+\delta(y+v-2),\quad 0<v,y\le 1,\end{aligned} \tag{A 2}$$

where Q is defined in equation (3.23) and T in equation (3.28). This expression was also derived in [11] for the eigenfunctions of that paper but again it holds for the current system. These results can be extended to EP3 (for which $Q=0$). It is found that

$$\begin{aligned}D_3(v,y)&=\sum_{n=2}^{\infty}\frac{Y_n(v)Y_n(y)}{P_n}+\frac{\xi(v)Y_1(y)+2\chi(y)\chi(v)+\xi(y)Y_1(v)}{R}-\frac{2U[\chi(v)Y_1(y)+Y_1(v)\chi(y)]}{R^2}\\&\quad+\frac{2U^2-WR}{R^3}Y_1(v)Y_1(y)+\frac{Y_0(v)Y_0(y)}{P_0}\\&=\delta(v-y)-\delta(v+y)+\delta(y+v-2),\quad 0<v,y\le 1,\end{aligned} \tag{A 3}$$

where U and W are given by equation (4.18) and R by equation (4.12).

Equations (A 1)–(A 3) can be used to demonstrate the loss of completeness of eigenfunctions $Y_n(y)$, $n=1,2,3,\ldots$ in the vicinity of an EP and that the additional functions do indeed restore completeness. While the following steps can be used to analyse any EP, the focus here is on the EP3 corresponding to the first row of table 1. To proceed, C_1 is perturbed very slightly while the other parameters remain the same. For these perturbations the roots α_1, α_2 and α_3 are very

Downloaded from http://royalsocietypublishing.org/rspa/article-pdf/doi/10.1098/rspa.2025.0811/6148136/rspa.2025.0811.pdf
by Brunel University user
on 05 July 2026

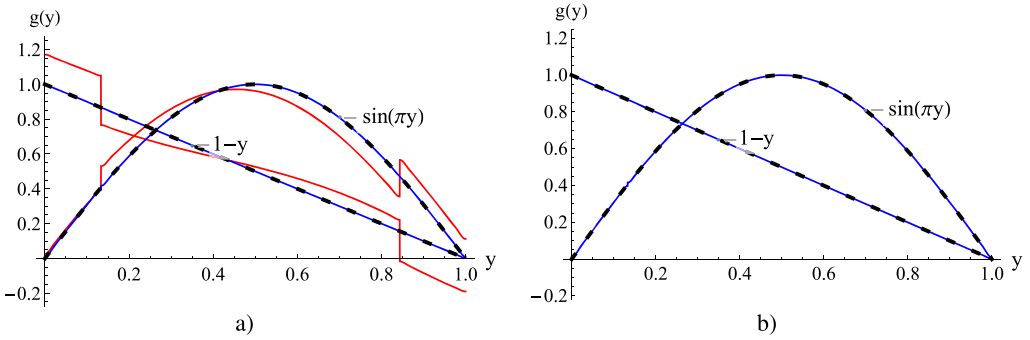

Figure 15. (a) Both sides of equation (A 4) at the parameters listed in the first row of table 1 but with $\mathcal{C}_1$ perturbed by adding 10^{-7} (blue curve) and 3×10^{-10} (red curve). (b) Verification of equation (A 4) (with $D_1(v, y)$ replaced by $D_3(v, y)$) at the EP3 parameters listed in the first row of table 1. In both (a) and (b), the test functions are $g(y) = \sin(\pi y)$ and $g(y) = 1 - y$ (the dashed curves) and the sum is truncated at 60 terms ($N = 60$).

close but not coincident so the perturbed parameters do not correspond to EP conditions and, in principle, equation (A 1) holds. On multiplying equation (A 1) by an arbitrary, suitably smooth function $g(v)$, $v \in (0, 1)$ and integrating across $0 \le v \le 1$ it is clear that

$$g(y) = \int_0^1 D_1(v, y) g(v)\, \mathrm{d}v, \quad 0 \le y \le 1. \tag{A 4}$$

Both sides of equation (A 4) are plotted in figure 15a for the test functions a) $g(y) = \sin(\pi y)$ and b) $g(y) = 1 - y$. It is clear that for a perturbation of 10^{-7} (blue curves) expression (A 4) holds for both of the chosen test functions, however, as the perturbation is reduced to 3×10^{-10} the identity fails (red curves) reflecting the impending loss of completeness of the eigenfunctions.

Now consider the situation exactly at EP3. If $D_1(v, y)$ in equation (A 4) is replaced with $D_2(v, y)$, the identity fails indicating that adding $\chi(y)$ to the set $Y_n(y)$, $n = 1, 2, 3, \ldots$ does not ensure completeness at EP3. (Indeed, at an EP3, the function $\chi(y)$ is orthogonal to $Y_1(y)$ and thus $Q = 0$ (see equation (3.23)) which guarantees the failure of $D_2(v, y)$ in this situation.) However, if $D_1(v, y)$ is replaced with $D_3(v, y)$ the left- and right-hand sides of the modified equation (A 4) agree, demonstrating that both $\chi(y)$ and $\xi(y)$ are needed to restore completeness at EP3. This is shown in figure 15b where the solid curves are the right-hand side of equation (A 4) and the dashed curves are the left-hand side for a) $g(y) = \sin(\pi y)$ and (b) $g(y) = 1 - y$. In this figure $N = 60$, that is, 60 terms are used in the summation. Thus, since two additional functions (generalized eigenfunctions) are required to restore completeness, it is confirmed that the parameters in the first row of table 1 correspond to an EP of order three.

References

1. Feng L, Zhu X, Yang S, Zhu H, Zhang P, Yin X, Wang Y, Zhang X. 2013 Demonstration of a large-scale optical exceptional point structure. *Opt. Express* **22**, 1760–1767. (doi:10.1364/OE.22.001760)
2. Zhao H, Chen Z, Zhao R, Feng L. 2018 Exceptional point engineered glass slide for microscopic thermal mapping. *Nat. Commun.* **9**, 1764. (doi:10.1038/s41467-018-04251-3)
3. Wiersig J. 2020 Review of exceptional point-based sensors. *Photon. Res.* **8**, 1457–1467. (doi:10.1364/PRJ.396115)
4. Even N, Nennig B, Lefebvre G, Perrey-Debain E. 2024 Experimental observation of exceptional points in coupled pendulums. *J. Sound Vib.* **575**, 118239. (doi:10.1016/j.jsv.2024.118239)
5. Ghienne M, Nennig B. 2020 Beyond the limitations of perturbation methods for real random eigenvalue problems using exceptional points and analytic continuation. *J. Sound Vib.* **480**, 115398. (doi:10.1016/j.jsv.2020.115398)

Downloaded from http://royalsocietypublishing.org/rspa/article-pdf/doi/10.1098/rspa.2025.0811/6148136/rspa.2025.0811.pdf
by Brunel University user
on 05 July 2026

6. Evans RB. 1992 The existence of generalized eigenfunctions and multiple eigenvalues in underwater acoustics. *J. Acoust. Soc. Am.* **92**, 2024–2029. (doi:10.1121/1.405254)
7. Erb J, Shaibe N, Calvo R, Lathrop DP, Antonsen Jr TM, Kottos T, Anlage SM. 2025 Topology and manipulation of scattering singularities in complex non-Hermitian systems: two-channel case. *Phys. Rev. Res.* **7**, 023090. (doi:10.1103/PhysRevResearch.7.023090)
8. Aurégan Y, Pagneux V. 2017 PT-symmetric scattering in flow duct acoustics. *Phys. Rev. Lett.* **118**, 174301.
9. Nashed MW, Elnady T, Åbom M. 2018 Modeling of duct acoustics in the high frequency range using two-ports. *Appl. Acoust.* **135**, 37–47.
10. Calmettes C, Perrey-Debain E, Lefrançois E, Caillet J. 2023 A multi-port scattering matrix formalism for the acoustic prediction in duct networks. *Acta Acust.* **7**, 13. (doi:10.1051/aacus/2023013)
11. Lawrie JB, Nennig B, Perrey-Debain E. 2022 Analytic mode-matching for accurate handling of exceptional points in a lined acoustic waveguide. *Proc. R. Soc. A* **478**, 20220484. (doi:10.1098/rspa.2022.0484)
12. Lawrie JB. 2013 Analytic mode-matching for acoustic scattering in three dimensional waveguides with flexible walls: application to a triangular duct. *Wave Motion* **50**, 542–557. (doi:10.1016/j.wavemoti.2012.12.002)
13. Lawrie JB, Guled IM. 2006 On tuning a reactive silencer by varying the position of an internal membrane. *J. Acoust. Soc. Am.* **120**, 780–790. (doi:10.1121/1.2213571)
14. Cremer L. 1953 Theory of sound attenuation in a rectangular duct with an absorbing wall and the resultant maximum attenuation coefficient. *Acustica* **2**, 249–263.
15. Tester BJ. 1973 The optimization of modal sound attenuation in duct, in the absence of mean flow. *J. Sound Vib.* **27**, 477–513. (doi:10.1016/S0022-460X(73)80358-X)
16. Zorumski WE, Mason JP. 1974 Multiple eigenvalues of sound-absorbing circular and annular ducts. *J. Acoust. Soc. Am.* **55**, 1158–1165. (doi:10.1121/1.1914680)
17. Koch W. 1977 Attenuation of sound in multi-element acoustically lined rectangular ducts in the absence of mean flow. *J. Sound Vib.* **52**, 459–496. (doi:10.1016/0022-460X(77)90365-0)
18. Qiu XH, Jing XD, Du L, Sun XF, Åbom M, Bodén H. 2020 Mode-merging design method for nonlocally reacting liners with porous materials. *AIAA J.* **58**, 2533–2545. (doi:10.2514/1.J058958)
19. Qiu X, Du L, Jing X, Sun X, Åbom M, Bodén H. 2020 Optimality analysis of bulk-reacting liners based on mode-merging design method. *J. Sound Vib.* **485**, 115581. (doi:10.1016/j.jsv.2020.115581)
20. Kabral R, Du L, Åbom M. 2016 Optimum sound attenuation in flow ducts based on the on the exact Cremer impedance. *Acta Acust. United Acust.* **102**, 851–860. (doi:10.3813/AAA.918999)
21. Qiu X, Du L, Jing X, Sun X. 2019 The Cremer concept for annular ducts for optimum sound attenuation. *J. Sound Vib.* **438**, 383–401. (doi:10.1016/j.jsv.2018.09.029)
22. Zhang Z, Bodén H, ébom M. 2019 The Cremer impedance: an investigation of the low frequency behavior. *J. Sound Vib.* **459**, 114844. (doi:10.1016/j.jsv.2019.07.010)
23. Xiong L, Nennig B, Aurégan Y, Bi W. 2017 Sound attenuation optimization using metaporous materials tuned on exceptional points. *J. Acoust. Soc. Am.* **142**, 2288–2297. (doi:10.1121/1.5007851)
24. Perrey-Debain E, Nennig B, Lawrie JB. 2022 Mode coalescence and the Green's function in a two-dimensional waveguide with arbitrary admittance boundary conditions. *J. Sound Vib.* **516**, 116510. (doi:10.1016/j.jsv.2021.116510)
25. Shenderov EL. 2000 Helmholtz equation solutions corresponding to multiple roots of the dispersion equation for a waveguide with impedance walls. *Acoust. Phys.* **46**, 357–363. (doi:10.1134/1.29892)
26. Kuznetsova S, Aurégan Y, Pagneux V. 2023 Higher-order mode filtering by a resistive layer. *JASA Express Lett.* **3**, 104001. (doi:10.1121/10.0021283)
27. Farooqui M, Aurégan Y, Pagneux V. 2022 Ultrathin resistive sheets for broadband coherent absorption and symmetrization of acoustic waves. *Phys. Rev. Appl.* **18**, 014007. (doi:10.1103/PhysRevApplied.18.014007)
28. Kuznetsova S, Aurégan Y, Pagneux V. 2024 Loss-induced modal selection by a resistive Wiremesh. *J. Acoust. Soc. Am.* **156**, 369–377. (doi:10.1121/10.0026541)
29. Eom HJ. 2004 *Electromagnetic wave theory for boundary-value problems*. An Advanced Course on Analytical Methods. Springer.

Downloaded from http://royalsocietypublishing.org/rspa/article-pdf/doi/10.1098/rspa.2025.0811/6148136/rspa.2025.0811.pdf
by Brunel University user
on 05 July 2026

30. Okoyenta AR, Wu H, Liu X, Jiang W. 2020 A short survey on Green's function for acoustic problems. *J. Theor. Comput. Acoust.* **28**, 1950025. (doi:10.1142/S2591728519500257)
31. Nennig B. 2025 A library to locate exceptional points from analytical dispersion equations. https://github.com/nennigb/dispyrsion/blob/master/examples/duct_with_wiremesh.py.
32. Warren DP, Lawrie JB, Mohamed IM. 2002 Acoustic scattering in waveguides that are discontinuous in geometry and material property. *Wave Motion* **36**, 119–142. (doi:10.1016/S0165-2125(02)00005-7)
33. Nawaz R, Lawrie JB. 2013 Scattering of a fluid-structure coupled wave at a flanged junction between two flexible waveguides. *J. Acoust. Soc. Am.* **134**, 1939–1949. (doi:10.1121/1.4817891)

Downloaded from http://royalsocietypublishing.org/rspa/article-pdf/doi/10.1098/rspa.2025.0811/6148136/rspa.2025.0811.pdf
by Brunel University user
on 05 July 2026